Cleaner Engineering and Technology 12 (2023) 100594

Contents lists available at ScienceDirect

Cleaner Engineering and Technology

journal homepage: www.sciencedirect.com/journal/cleaner-engineering-and-technology

Agrivoltaic system: Estimation of photosynthetic photon flux density under solar panels based on solar irradiation data using all-climate solar spectrum model

Daisuke Yajima [a], Teruya Toyoda [b], Masaaki Kirimura [a,c], Kenji Araki [d], Yasuyuki Ota [a,b,d,*], Kensuke Nishioka [a,b,d]

[a] Interdisciplinary Graduate School of Agriculture and Engineering, University of Miyazaki, 1-1 Gakuen Kibanadai-nishi, Miyazaki, 889-2192, Japan
[b] Graduate School of Engineering, University of Miyazaki, 1-1 Gakuen Kibanadai-nishi, Miyazaki, 889-2192, Japan
[c] Faculty of Agriculture, University of Miyazaki, 1-1 Gakuen Kibanadai-nishi, Miyazaki, 889-2192, Japan
[d] Faculty of Engineering, University of Miyazaki, 1-1 Gakuen Kibanadai-nishi, Miyazaki, 889-2192, Japan

ARTICLE INFO

Keywords:
Agrivoltaic system
Farming photovoltaics
Solar radiation
Climate change
Increasing food production
Photosynthetic photon flux density

ABSTRACT

Climate change and increasing food production due to population growth are global challenges that need immediate attention. The introduction of renewable energy to mitigate climate change and the requirement of adequate land to increase food production are generally mutually exclusive. However, an agrivoltaic system generates renewable electricity and produces agricultural products from a common piece of land, thus increasing the land productivity. In addition, this system contributes to local production, thus reducing the CO_2 emissions from logistics. Photovoltaic arrays in previous studies were designed by calculating the irradiance in W/m^2, even in recent studies. A careful design of the farmland's illumination must be developed for effective agriculture. The simulations must be scaled based on photosynthetic photon flux density rather than irradiance commonly applied in photovoltaic technology simulations.

This study focused on the photosynthetic photon flux density and employed an all-climate solar spectrum model to calculate the photosynthetic photon flux density accurately on farmland partially shaded by solar panels and supporting tubes. This study described an algorithm for estimating the photosynthetic photon flux density values under solar panels. The calculated data were validated using the photosynthetic photon flux density sensors. To calculate the photosynthetic photon flux density under the solar panels, it is essential to weigh the direct and diffused components shaded by the solar panels separately because they have different spectrums. A method to quantify the shading was explored here by solar panels and their supporting tubes for the direct and diffused component as the sun moves. The calculation formula was established by defining the sun's moves and the positions of solar panels and their supporting tubes in terms of elevation and azimuth angles from the observation point.

It was found that the waveform based on the calculation formula for the photosynthetic photon flux density under the solar panels reproduced the same tendency as the measured photosynthetic photon flux density. To evaluate this trend numerically, the measured and calculated photosynthetic photon flux densities were compared using the standard residuals. Generally, the similarity of the two values is confirmed by a standard residual value between −3 and 3. The result of this study showed that the standard residual values were negative in more frequencies except for the zero photosynthetic photon flux density at night. This indicates that the calculated photosynthetic photon flux density tends to be higher than the measured photosynthetic photon flux density. The peak frequency of the standard residuals was between −6 and −3. This difference probably occurred because the established calculation formula targets the shading provided by the solar panels and supporting tubes but does not cover the shading provided by the other system structures. The calculation formula enables farmers to evaluate the economic efficiency of the system before introducing it using measured solar irradiation data at the target farmlands by introducing published neighborhood solar irradiation data and considering, in

Abbreviations: ACSS, All-climate solar spectrum; METPV-11, MEteorological Test data for Photovoltaic systems; PPFD, Photosynthetic photon flux density.

* Corresponding author. Interdisciplinary Graduate School of Agriculture and Engineering, University of Miyazaki, 1-1 Gakuen Kibanadai-nishi, Miyazaki, 889-2192, Japan.
E-mail address: y-ota@cc.miyazaki-u.ac.jp (Y. Ota).

https://doi.org/10.1016/j.clet.2022.100594
Received 24 August 2022; Received in revised form 15 November 2022; Accepted 30 November 2022
Available online 5 December 2022

advance, measures to avoid the effects of shading on agricultural production. The next study will be to improve the accuracy of the calculation formula by increasing the number of days and develop a method that leads to the best practices of agricultural production and solar power generation by introducing the system.

Nomenclature

g_j	Center position of the solar panel
j	Number of solar panels ($0 = j \leq 13$)
q_i	Observation point
i	Mesh line number of observation points on the cultivated land ($0 = i \leq 800$)
t	Sampled parameters of time/date
S_n	Space between solar panels ($0 = n \leq 8$)
PPFDus	PPFD under solar panels
PPFDd	PPFD from direct solar irradiation
PPFDs	PPFD from sources other than direct solar irradiation, including diffused solar irradiation
Rs	Shading rate for direct solar irradiation
RS1	Shading rate for direct solar irradiation by solar panels
RS2	Shading rate for direct solar irradiation by supporting tubes
Ω	Ski-shielding rate for irradiations other than direct solar irradiation, including diffused solar irradiation
αt	Amplitude angle of the sun at time "*t*" ($-90° = \alpha t \leq 90°$)
ν	Elevation angle of diffused sunlight ($0° \; ? \; \nu \leqq 90°$)
φ	Azimuthal angle of diffused sunlight ($-180° \; ? \; \varphi \leqq 180°$)
x1ij	Distance on the x-axis from the observation point "*i*" to the lower end of solar panel "*j*"
x2ij	Distance on the x-axis from the observation point "*i*" to the top of solar panel "*j*"
x11ij	Distance on the x-axis from the observation point "*i*" to the lower end of torque tube "*j*"
x21ij	Distance on the x-axis from the observation point "*i*" to the top of torque tube "*j*"
(yij)t	Distance on the y-axis from the observation point "*i*" to the point where the incident light intersects the center of the solar panel "*j*" in the x-axis direction at time "*t*"
z1	Distance on the z-axis from the observation point "*i*" to the lower end of solar panel "*j*"
z2	Distance on the z-axis from the observation point "*i*" to the top of solar panel "*j*"
z11	Distance on the z-axis from the observation point "*i*" to the lower end of torque tube "*j*"
z21	Distance on the z-axis from the observation point "*i*" to the top of torque tube "*j*"
H	Vertical width of the solar panel
Ht	Vertical width of the torque tube
h	Installation height of the solar panel from the observation point
ΦΦ	Installation angle of the solar panel
Πt	Elevation angle of the sun at time "*t*"
(θ1ij)t	Elevation angle of the bottom of the solar panel at time "*t*"
(θ2ij)t	Elevation angle of the top of the solar panel at time "*t*"
(θ11ij)t	Elevation angle of the bottom of the solar panel at time "*t*"
(θ21ij)t	Elevation angle of the top of the solar panel at time "*t*"
θ1sij	Elevation angle of the bottom of the solar panel
θ2sij	Elevation angle of the top of the solar panel

1. Introduction

Climate change and increasing food production due to population growth are global challenges that need immediate attention. For example, the effects of population growth and climate change in Africa are exacerbated by the limitations of traditional low-productivity open-field crop and grain-fed production systems. Despite the introduction of greenhouse technology to provide a sustainable year-round vegetable supply, vegetable imports continue to increase, and research is underway to find solutions for Ghana (Forkuor et al., 2022). Vertical farming methods have been introduced to use farmland efficiently, and research is underway to establish design methods for maximum efficiency (Choubchilangroudi and Zarei, 2022). To mitigate the effects of agriculture on climate change, a previous study considered using solar power to drive the pumping systems used in Australia's vast sugarcane plantations (Powell et al., 2021).

The agrivoltaic system advocated by Dupraz et al. (2011) involves the cultivation of agricultural products on farmland and generation of electricity using solar panels installed approximately 3 m above the farmland. This system can simultaneously solve two major global challenges by generating renewable energy and producing food from a single land. Abidin et al. (2021) proposed two additional requirements of ensuring adequate water supply to the crops by maintaining the soil moisture and ensuring a stable environment under the solar panels.

For the efficient use of the photovoltaic system, Hassan et al. (2022) increased the self-sufficiency rate from 28.09% to 40.77% with electricity supplied solely from the solar power system using a supercapacitor module. Several studies have installed hydrogen storage systems to promote the efficient use of photovoltaic systems. One study focused on system degradation and proposed the unit additional hydrogen consumption ratio as an indicator to measure the overall degradation of the system, and identified that, after 10 years, the unit additional hydrogen consumption ratio increased by 33.2–36.2% compared to the initial state (Ceran et al., 2021). Although not in the agricultural field, a study on the combination of a photovoltaic system and a hydrogen storage system established a numerical analysis method to optimize the fuel cell capacity and increase the renewable energy ratio to achieve the desired electricity load; the case study considered an ordinary household connected to the grid (Hassan, 2020).

The development of agrivoltaic systems was motivated primarily by the generation of photovoltaic energy in farmlands with constraints, that is, this system provides farmers with income from selling agricultural products in addition to income from power generation on the same land. This new source of income helps mitigate the loss in agricultural income due to volatile climate and market risk (Cuppari et al., 2021). Nordberg et al. (2021) also mentioned that environmental credit indirectly affects carbon sequestration and biodiversity improvements.

Many researchers have analyzed the effects of the agrivoltaic system on communities in Japan (Irie et al., 2019), the United States (Pascaris et al., 2021), Palestine (Braik et al., 2021), Spain (Moreda et al., 2021), Germany (Trommsdorff et al., 2021a), Turkey (Coşgun, 2021), Europe (Willockx et al., 2020), the Russian Federation (Kostik et al., 2020), India (Trommsdorff et al., 2021b), Thailand (Kumpanalaisatit et al., 2022), and East Africa (Randle-Boggis et al., 2021). Toledo and Scognamiglio (2021) mentioned the importance of consideration of the local landscape before installing the agrivoltaic system.

Some researchers have examined the effects of the agrivoltaic system

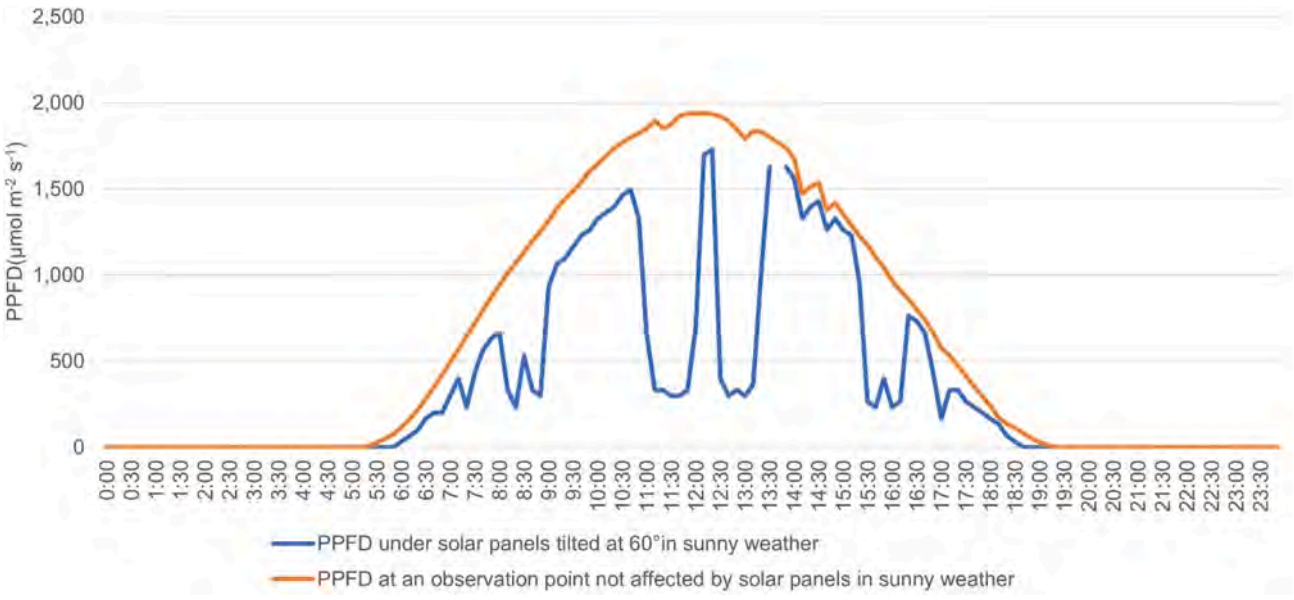

Fig. 1. Comparison of measured PPFDs above and under solar panels (the data at 13:40 are missing) on May 29, 2017.

Fig. 2. Agrivoltaic system at the University of Miyazaki.

on a global scale. Adeh et al. (2019) described the potential of the agrivoltaic system to offset the world's energy needs by introducing it to less than 1% of agricultural land. Schindele et al. (2020) examined the effectiveness of the agrivoltaic system in multiple countries for solving the problem of land competition between agriculture and power generation.

In the abovementioned studies, the reported effects of installing solar panels on agricultural growth are site-specific; hence, although their results are informative, the studies are not useful for decision-making by farmers and businesses located in other geographical areas. Farmers and businesses considering the introduction of the agrivoltaic system need quantitative data on power generation and agricultural production in their specific areas of interest.

It is necessary to optimize solar resource usage for photovoltaics while maintaining sufficient illumination on the farmland (Beck et al., 2012). Therefore, photovoltaic arrays were designed by calculating the irradiance measured in W/m^2, even in recent studies (Perna et al., 2019). Furthermore, the system design was neither specific to the local climate conditions nor was it geographically generalized.

However, the illumination on the farmland must be carefully designed to support agriculture. The simulations must be conducted in terms of the photosynthetic photon flux density (PPFD) rather than the irradiance used commonly in photovoltaic technology simulations. Further, it is essential to estimate the PPFD under the solar panel instead of that above the solar panel to predict agricultural production accurately. A comparison between the PPFD measured above and under the solar panels is shown in Fig. 1.

For highly accurate control of the illumination in farmland, detailed calculations performed by considering local climate conditions at different times of the year and their validations are crucial. However, this increases the computation substantially. Therefore, it is necessary to develop a generalized model using nondimensional parameters and link it to the climate and solar databases. This has the advantage of less calculation time, leading to ease of integration with respect to time (time in days, months, and seasons) and area.

For conversion to PPFD, the accurate calculation of the solar spectrum is essential to predict the photon numbers. Most studies attempting to develop a solar spectrum model have assumed clear-sky conditions. This situation is considered acceptable in the computation of photovoltaic energy yield because photovoltaic systems receive the maximum solar energy on clear-sky days (Tobiska et al., 2000). Moreover, the solar spectrum model was developed under clear-sky conditions (Gregg and Carder, 1990). In contrast, the spectrum weighting for the PPFD in the solar panel shadow requires an accurate spectrum in diffused sunlight. Therefore, the illumination spectrum in an overcast climate is crucial. Our group recently succeeded in developing an all-climate solar spectrum (ACSS) model and predicting the performance of a spectrum-sensitive triple-junction photovoltaic module with a fixed slope angle (Tawa et al., 2020).

The novelty of this study was the establishment of a calculation formula for estimating PPFD under solar panels employing the ACSS

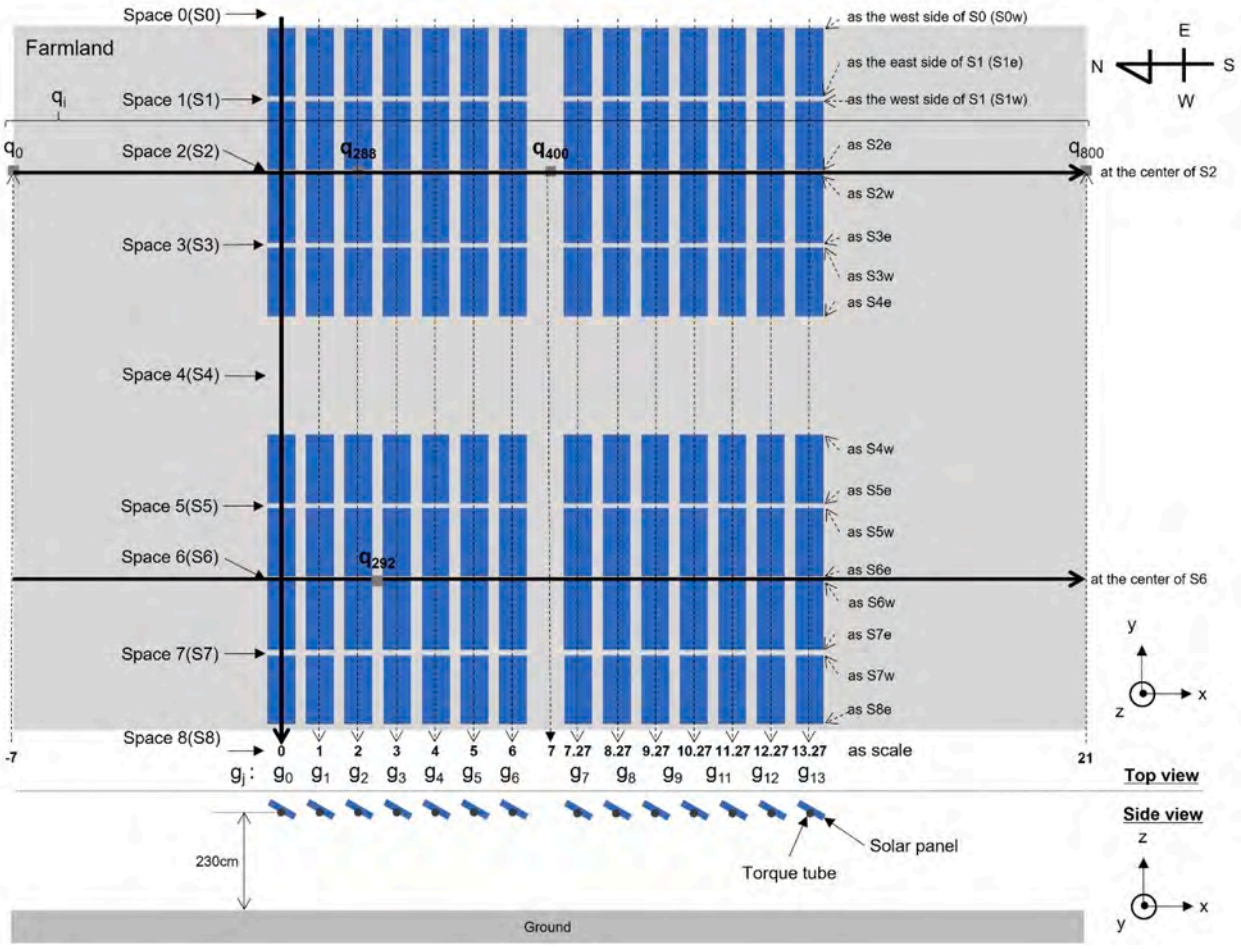

Fig. 3. Schematic of the top and sides of the entire testing zone.

Table 1
Dimensionless scales.

Items	Length/Height/ Width	Dimensionless scale
Length between centers of the solar panels	73 cm (Standard scale)	1
Width of solar panel	55 cm	0.753
Length of solar panel	240 cm	3.288
Diameter of supporting tube	5 cm	0.068
Height from PPFD sensor to center of solar panel	230 cm	3.151
Width of spaces 1, 2, 3, 5, 6, and 7	34 cm	0.466
Width of space 4	600 cm	8.219

model. An algorithm for estimating the PPFD values under the solar panels was described. The calculated data were validated using PPFD sensors. To calculate the PPFD under the solar panels, it is essential to weigh the direct and diffused components shaded by the solar panels separately because they have different spectrums. A method to quantify the shading by solar panels and their supporting tubes for the direct and diffused component as the sun moves was explored here. The calculation formula was established by defining the sun's moves and the positions of solar panels and their supporting tubes in terms of elevation and azimuth angles from the observation point.

The calculation formula enables farmers to evaluate the economic efficiency of the system before introducing it using measured solar irradiation data at the target farmlands by introducing published neighborhood solar irradiation data and to consider in advance measures to avoid the effects of shading on agricultural production.

2. Methods

2.1. Design philosophy of agrivoltaic system

The estimation of the PPFD is essential for the accurate prediction of crop yield. Precise modeling of the spectrum is indispensable for predicting the number of photons. Furthermore, the calculated PPFD under the solar panels must be easily applicable to predict the crop yield by controlling the shading ratio using solar panels. This study describes an algorithm for estimating the PPFD values under solar panels. The calculated data are validated using PPFD sensors. The validated PPFD prediction model under the solar panel will help in designing an agrivoltaic system with simultaneous maximization of electricity and crop yield.

2.2. Demonstration of agrivoltaic system

An array of photovoltaic systems with an adjustable slope angle was installed on farmland used for growing taro (*Colocasia esculenta* Schott) at the University of Miyazaki (N31.83°, E131.41°), as shown in Fig. 2.

All solar panels were mounted on supporting tubes that could be rotated manually and adjusted to balance the solar irradiance and crop yield. The schematic of the top and sides of the entire testing zone are shown in Fig. 3.

The center position of the solar panel is at g_j ($0 = j \leq 13$), and q_i ($0 = i \leq 800$) is the observation point. q_{288} and q_{292} correspond to various sensors installed for comparing the calculated data with the measured data. Each geometrical variable was converted into a dimensionless scale to support a generalized discussion and to save calculation time. In

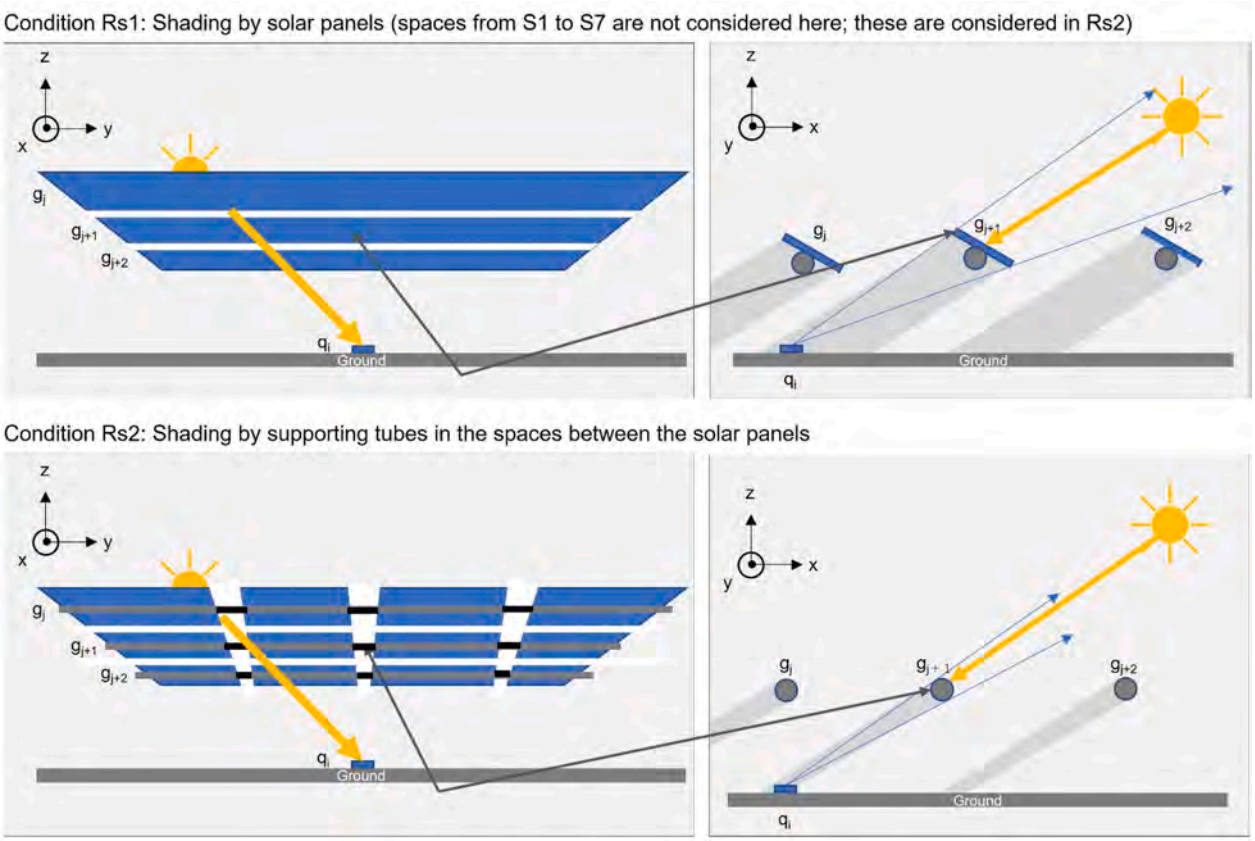

Fig. 4. Conceptual diagrams of *Rs1* and *Rs2*.

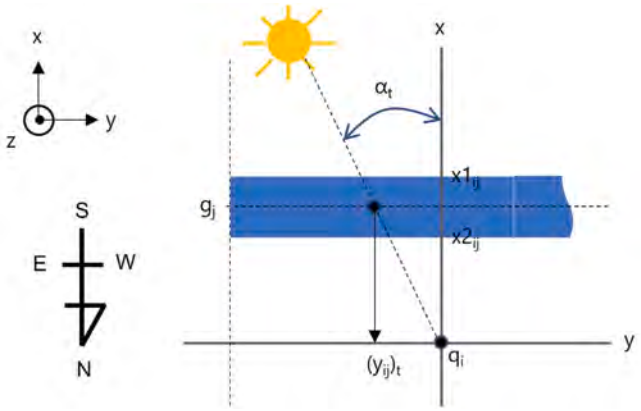

Fig. 5. Positional relationship between direct sunlight and solar panel from the viewpoint of the azimuth angles, as seen at the observation point.

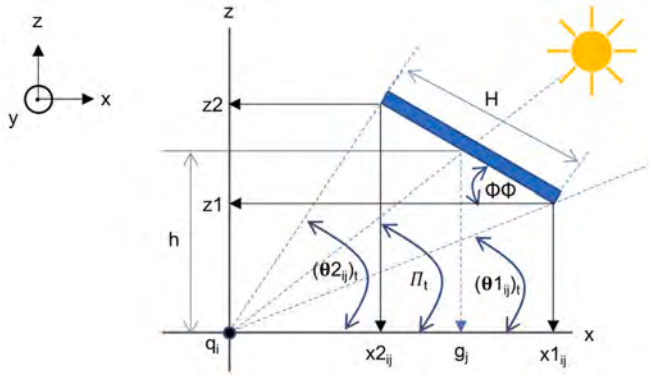

Fig. 6. Positional relationship between direct sunlight and solar panel from the viewpoint of the elevation angles, as seen at the observation point.

this study, the 1 (one) dimensionless scale of 73 cm was used based on the length between the centers of the solar panels. Table 1 lists the dimensionless scales.

2.3. Algorithm for calculation of PPFD under solar panels considering climatic conditions

The direct and diffused (normal or horizontal plane) components of the solar irradiance were collected; the irradiance values varied with time and season. The irradiance data may be obtained through outdoor measurements in an open space or from a solar database containing direct and diffused solar irradiances. The measurements at every 10 s were used in this study. The typical time-step of the solar resource database is 1 h, including that in the METPV-11 (MEteorological Test data for Photovoltaic systems, developed in 2011) (Itagaki et al., 2003).

The target land was divided into 800 mesh lines denoted by i in Fig. 3. Illumination by both direct and diffused sunlight can be calculated at every mesh line.

To calculate the PPFD under the solar panels, it is essential to weigh the direct and diffused components shaded by the solar panels separately because they have different spectrums. The PPFD under the solar panels at the given mesh line and time/date can be calculated by weighting the direct and diffused sunlight. The equation is as follows.

$$PPFDus_{it} = Rs_{it}\ PPFDd_{it} + (1 - \Omega_i)\ PPFDs_i, \quad (1)$$

where *PPFDus* is the PPFD under the solar panel, *PPFDd* is the PPFD from direct solar irradiation, and *Rs* is the shading rate for direct solar

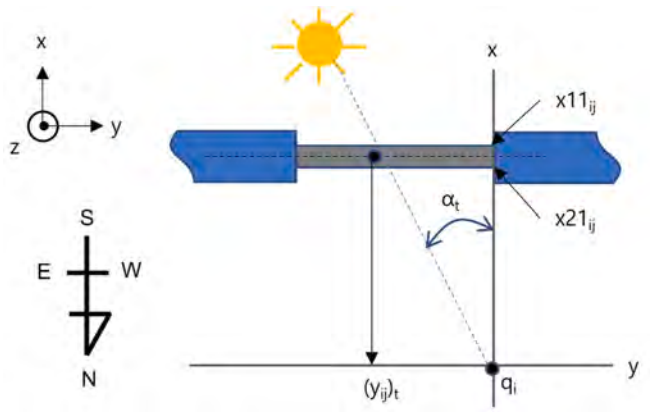

Fig. 7. Positional relationship between direct sunlight and supporting tube from the viewpoint of the azimuth angles, as seen at the observation point.

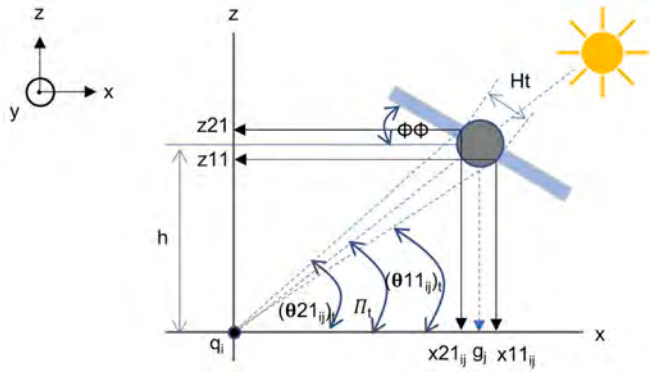

Fig. 8. Positional relationship between direct sunlight and supporting tube from the viewpoint of the elevation angles, as seen at the observation point.

irradiation, which is zero when direct sunlight is blocked and 1 (one) when not blocked. *PPFDs* is the PPFD from sources other than direct solar irradiation, including diffused solar irradiation, and Ω is the ski-

Table 2
Relationship between wavelength and extraterrestrial spectrum, given by Bird and Riordan (abstracted; the original table shows 122 wavelengths).

K	Wavelength (μm)	Extraterrestrial spectrum ($Wm^{-2}μm^{-1}$)
0	0.300	535.9
15	0.400	1479.1
37	0.690	1420.0
38	0.710	1399.0
121	8.6	0.045

Source: Table 1 from Simple Solar Spectral Model for Direct and Diffuse Irradiance on Horizontal and Tilted Planes at the Earth's Surface for Cloudless Atmospheres (Bird and Riordan, 1986)

Fig. 10. Pyranometer used for global total irradiance measurement.

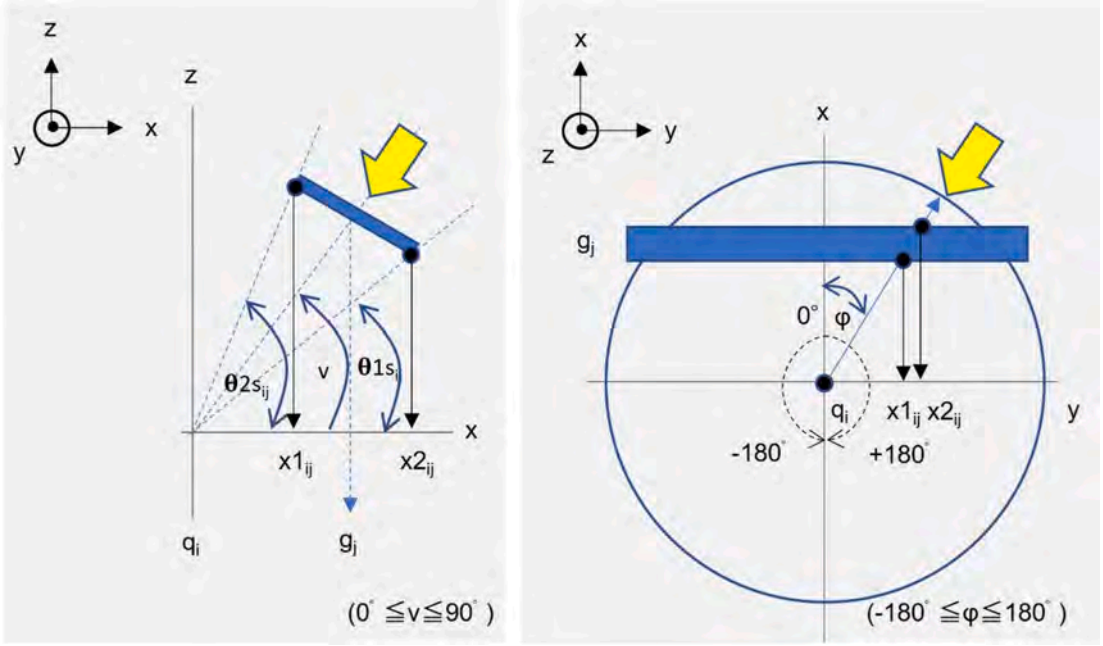

Fig. 9. Positional relationship between diffused sunlight and solar panels from the viewpoint of the azimuth and elevation angles, as seen at the observation point.

Fig. 11. Pyrheliometer with a 2-axis tracker for measurement of direct normal irradiance.

Fig. 12. Spectroradiometers for measurement of solar spectrum.

Fig. 13. PPFD sensor.

Table 3
Six patterns.

Pattern no.	Panel angles and observation point	Weather pattern and measurement date
1	Observation point under solar panels with solar panel angle of 0°	Sunny weather on May 29, 2017
2	Observation point under solar panels with solar panel angle of 60°	
3	Observation point not affected by solar panels	
4	Observation point under solar panels with solar panel angle of 0°	Cloudy weather on May 31, 2017
5	Observation point under solar panels with solar panel angle of 60°	
6	Observation point not affected by solar panels	

shielding rate for sources other than direct solar irradiation, including diffused solar irradiation. The suffixes *i* and *t* correspond to the mesh line number on the cultivated land and sampled parameters of the time/date, respectively. Each suffix originates from 0. The suffix *i* starts and proceeds from the south end.

2.3.1. Calculation model of shading rate for direct solar irradiation (Rs)

RS is a logical function and consists of shading by solar panels (*Rs1*) and shading by supporting tubes (*Rs2*). The relationship between *Rs1* and *Rs2*, as seen at the observation point, is shown in Fig. 4. First, the horizontal shading of the solar panel was calculated with *Rs1*, and then the vertical spaces between the solar panels were calculated with *Rs2* considering the shading effect of the supporting tube.

Rs is the logical product for the entire panel, obtained as the logical sum of the shading by the solar panels and that by the supporting tubes. The equation is as follows.

$$Rs_{it} = \prod_{j}\left(\left(Rs1_{ij}\right)_t \vee \left(Rs2_{ij}\right)_t\right) \tag{2}$$

The positional relationship between direct sunlight and the solar panel from the viewpoint of the azimuth angles, as seen at the observation point, is shown in Fig. 5, whereas that from the viewpoint of the elevation angles is seen in Fig. 6. In this study, the skew angle was assumed to be zero. If the skew angle is taken into consideration, it is necessary to subtract it from α_t.

The positional relationship between direct sunlight and the supporting tube from the viewpoint of the azimuth angles, as seen at the observation point, is shown in Fig. 7, whereas that from the viewpoint of the elevation angles is shown in Fig. 8.

Rs1 determines whether the elevation angle of sunlight (Π) is between the top ($\theta 2$) and bottom ($\theta 1$) of the solar panel and whether the azimuth (y) is between the east ($S0w$) and west ($S8e$) of the solar panels. Similarly, *Rs2* determines whether the elevation angle of sunlight (Π) is between the top ($\theta 21$) and bottom ($\theta 11$) of the supporting tube and whether the azimuth (y) is between the east and west of each space from *S1* to *S7* between the solar panels. In the logical formula, the value one is returned when the condition is met, but a negative symbol is added to make it zero in the PPFD calculation. The equations are as follows.

$$\left(Rs1_{ij}\right)_t = \neg\left(\left(\theta 1_{ij}\right)_t < \Pi_t < \left(\theta 2_{ij}\right)_t\right) \wedge \left(S0w < \left(y_{ij}\right)_t < S8e\right) \tag{3}$$

$$\left(Rs2_{ij}\right)_t = \left(\neg\left(\left(\theta 11_{ij}\right)_t < \Pi_t < \left(\theta 21_{ij}\right)_t\right)\right) \wedge \left(\left(S1e < \left(y_{ij}\right)_t < S1w\right) \vee \cdots \vee \left(S7e < \left(y_{ij}\right)_t < S7w\right)\right) \tag{4}$$

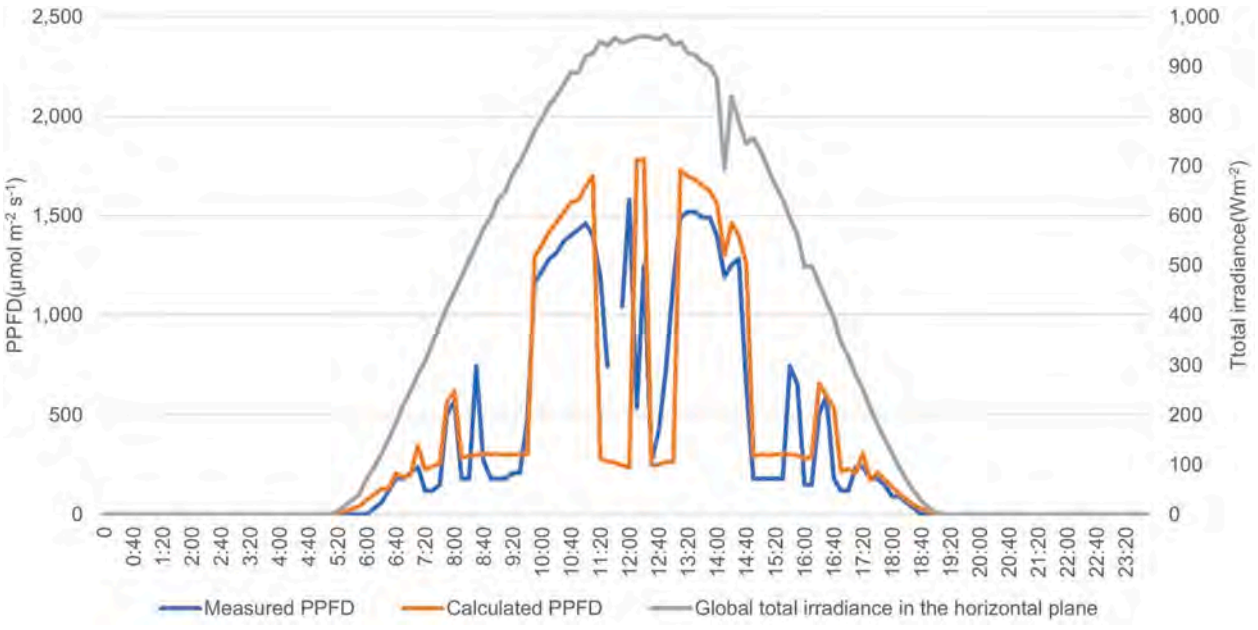

Fig. 14. Comparison of measured and calculated PPFDs and global total irradiance in the horizontal plane for solar panel angle of 0° in sunny weather on May 29, 2017 (data at 11:40 are missing).

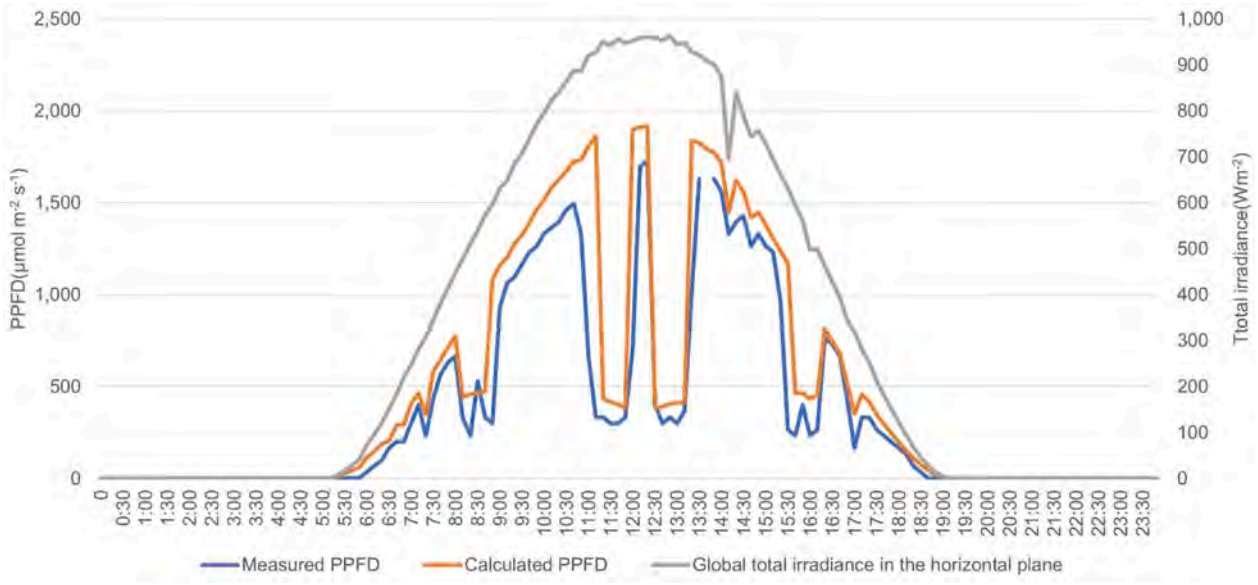

Fig. 15. Comparison of measured and calculated PPFDs and global total irradiance in the horizontal plane for solar panel angle of 60° in sunny weather on May 29, 2017 (data at 13:40 are missing).

$$\left(\theta 1_{ij}\right)_t = if\left(x1_{ij} = 0, 90\ deg, \tan^{-1}\left(\frac{z1\cos\alpha_t}{x1_{ij}}\right)\right) \quad (5)$$

$$x1_{ij} = -q_i + 0.5H\cos\Phi\Phi + g_{\,j} - 0.5N \quad (6)$$

$$z1 = h - 0.5H\sin\Phi\Phi \quad (7)$$

$$\left(\theta 2_{ij}\right)_t = if\left(x2_{ij} = 0, 90\ deg, \tan^{-1}\left(\frac{z2\cos\alpha_t}{x2_{ij}}\right)\right) \quad (8)$$

$$x2_{ij} = -q_i - 0.5H\cos\Phi\Phi + g_{\,j} - 0.5N \quad (9)$$

$$z2 = h + 0.5H\sin\Phi\Phi \quad (10)$$

$$\left(\theta 11_{ij}\right)_t = if\left(x11_{ij} = 0, 90\ deg, \tan^{-1}\left(\frac{z11\cos\alpha_t}{x11_{ij}}\right)\right) \quad (11)$$

$$x11_{ij} = -q_i + 0.5Ht\cos\Phi\Phi + g_{\,j} - 0.5N \quad (12)$$

$$z11 = h - 0.5Ht\sin\Phi\Phi \quad (13)$$

$$\left(\theta 21_{ij}\right)_t = if\left(x21_{ij} = 0, 90\ deg, \tan^{-1}\left(\frac{z21\cos\alpha_t}{x21_{ij}}\right)\right) \quad (14)$$

$$x21_{ij} = -q_i - 0.5Ht\cos\Phi\Phi + g_{\,j} - 0.5N \quad (15)$$

$$z21 = h + 0.5Ht\sin\Phi\Phi \quad (16)$$

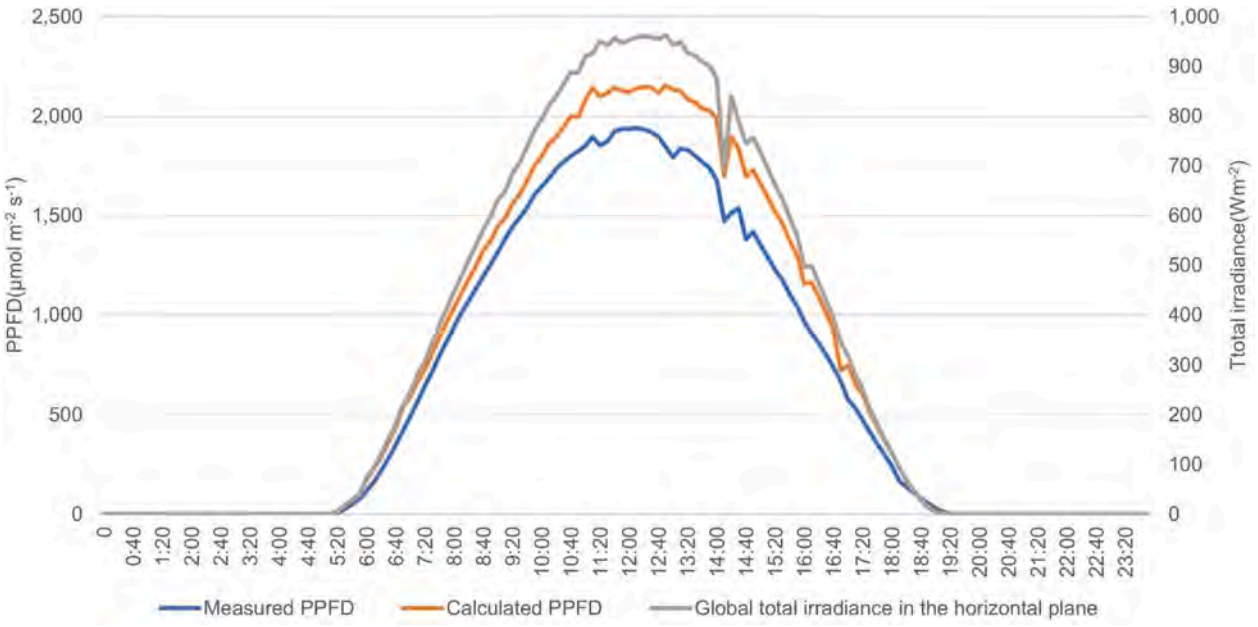

Fig. 16. Comparison of measured and calculated PPFDs and global total irradiance in the horizontal plane at the observation point not affected by solar panels in sunny weather on May 29, 2017.

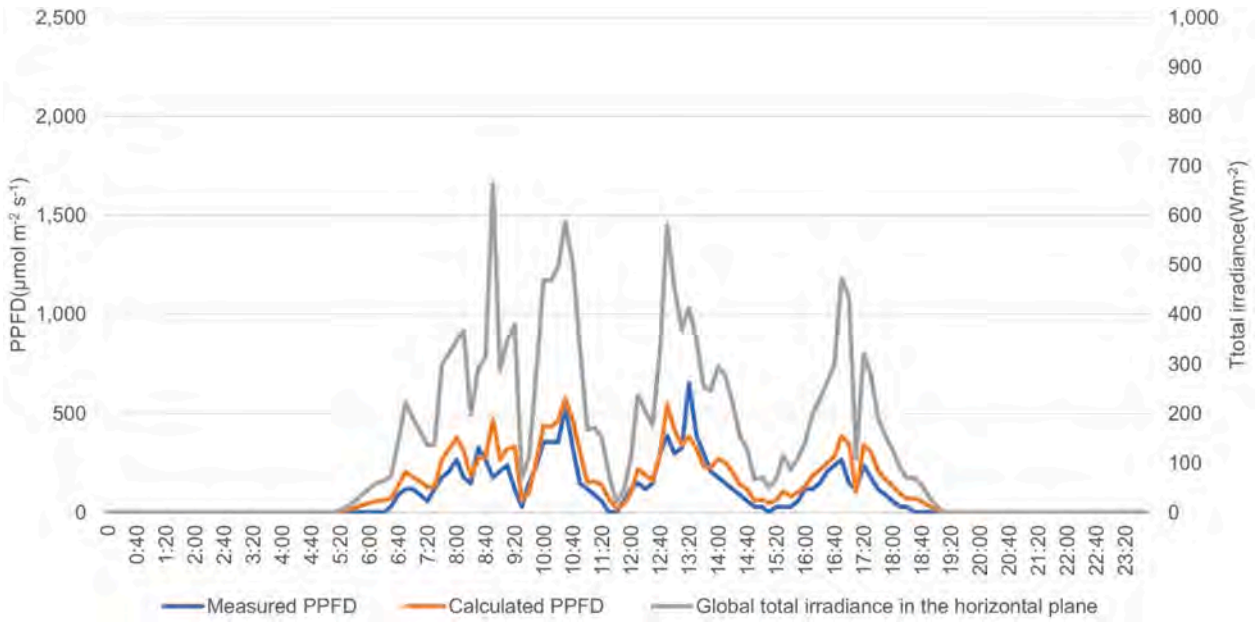

Fig. 17. Comparison of measured and calculated PPFDs and global total irradiance in the horizontal plane for solar panel angle of 0° in cloudy weather on May 31, 2017.

$$\left(y_{ij}\right)_t = \left(\frac{x1_{ij} + x2_{ij}}{2}\right)\tan\alpha_t \tag{17}$$

N is the number of rows of solar panels installed ($N = 14$ in this study). In the formulas for calculating $x1$, $x2$, $x11$, and $x21$, $-0.5\,N$ was added because the observation point q_{400} sets the center on the x-axis.

Regarding $Rs1$, the equation considers y_{ij} in the azimuth direction, but obstacles such as school buildings were erected in the east and west of the system installed at the University of Miyazaki. Hence, the time from sunrise to the time when the sunrays reached the eastern end of the solar panel and the time from when the sunrays reached the western end to the time of sunset were judged based on only the elevation angle without considering y_{ii} because the incident light was blocked.

2.3.2. Calculation model of ski-shielding rate for diffused solar irradiation (Ω)

Ω is calculated using a logical function that considers a hemisphere centered at the observation point. First, the shading of diffused light in the elevation direction is checked by each 1° in the range from 0° to 90°; next, the shading of diffused light in the azimuth direction is checked by each 1° in the range from −180° to 180°

In this study, the calculation method does not consider spaces because the amount of solar radiation of scattered light is smaller than that of direct light to avoid complicated calculation. The positional relationship between diffused sunlight and solar panels from the viewpoint of the azimuth and elevation angles, as seen at the observation point, is shown in Fig. 9.

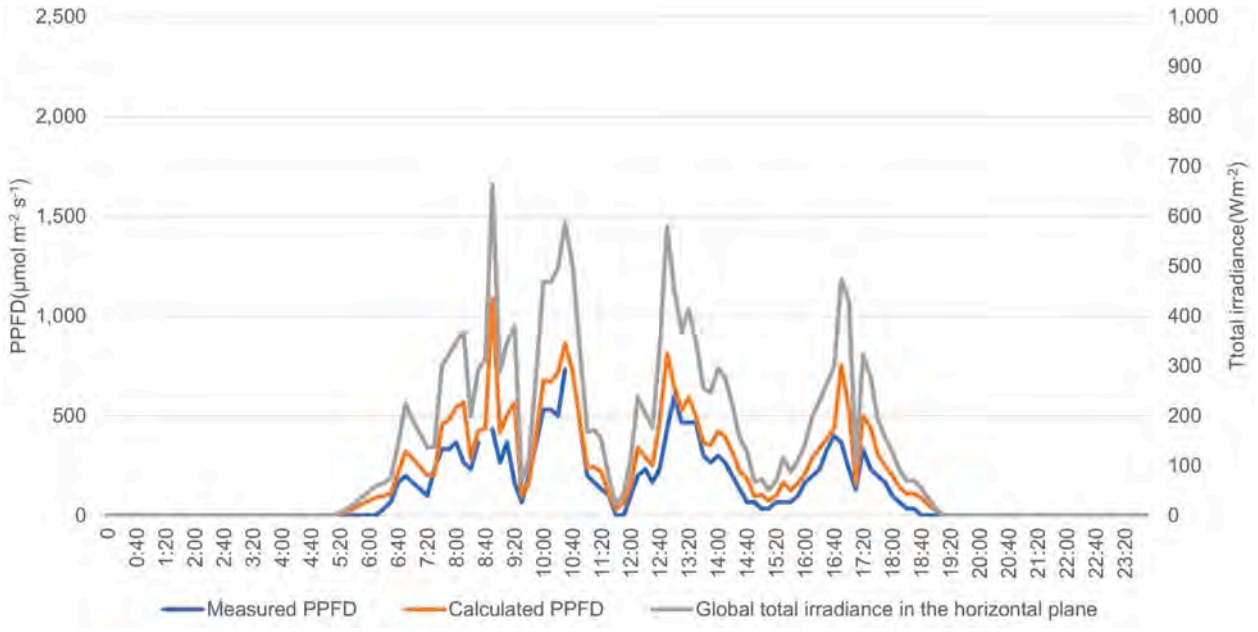

Fig. 18. Comparison of measured and calculated PPFDs and global total irradiance in the horizontal plane for solar panel angle of 60° in cloudy weather (data at 08:40 and 10:40 are missing) on May 31, 2017.

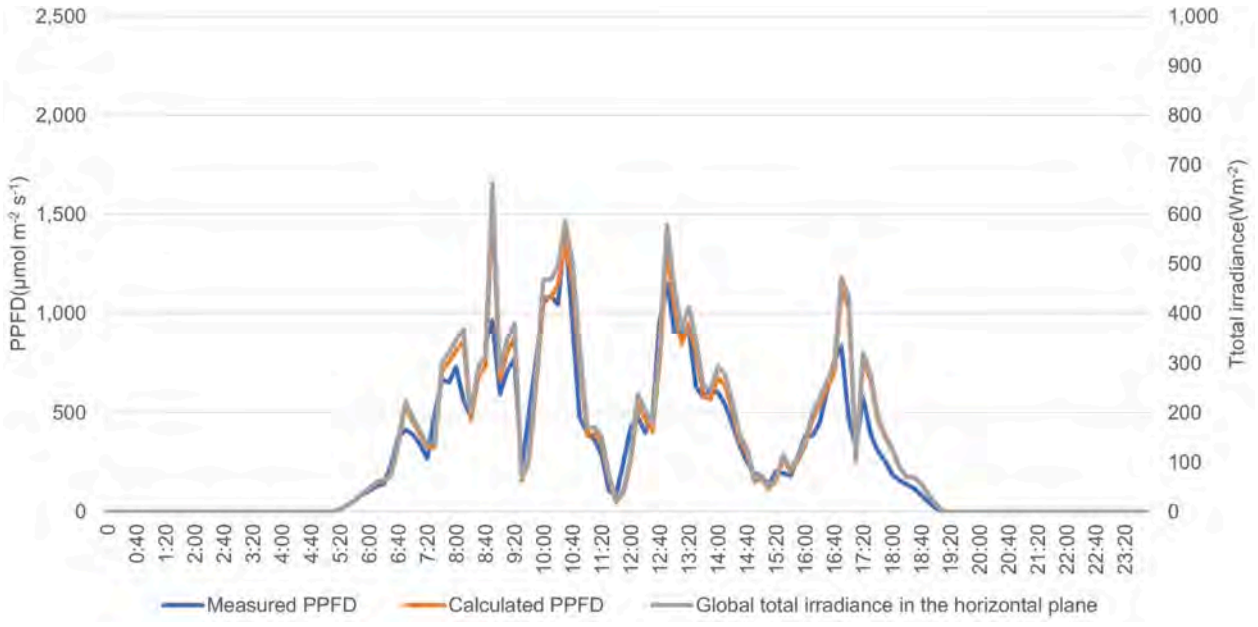

Fig. 19. Comparison of measured and calculated PPFDs and global total irradiance in the horizontal plane at the observation point not affected by solar panels in cloudy weather (data at 08:30 are missing) on May 31, 2017.

Ω is calculated as a fraction as follows.

$$\Omega_i = \int_{-180}^{180}\int_{0}^{90}\left(\sum_j\left(\left(median\left(\theta 1s_{ij},\theta 2s_{ij},v\right)=v\right)>0\right)\right)\frac{\delta v \bullet \delta\varphi}{90\ \text{deg} \bullet 360\ deg} \tag{18}$$

$$\theta 1s_{ij} = if\left(x1_{ij}=0,0,\tan^{-1}\left(\frac{z1\cos\varphi}{x1_{ij}}\right)\right) \tag{19}$$

$$\theta 2s_{ij} = if\left(x2_{ij}=0,0,\tan^{-1}\left(\frac{z2\cos\varphi}{x2_{ij}}\right)\right) \tag{20}$$

$$\delta v = 1\ \text{deg} \tag{21}$$

$$\delta\varphi = 1\ \text{deg} \tag{22}$$

2.3.3. Calculation of PPFDd and PPFDs

PPFDd and *PPFDs* are calculated using the solar irradiance data, which can be collected through measurements or can be obtained from the publicly available METPV-11 database. The calculation involves applying a trapezoid formula to the dataset given by Bird and Riordan (1986). The original model by the authors did not consider the fluctuation of the atmospheric parameters and ignored the sky conditions on clear-sky days. Tawa et al. (2020) developed a solar irradiation calculation model by considering the fluctuation of the atmospheric parameters and ignoring the sky conditions on clear-sky days. In this study,

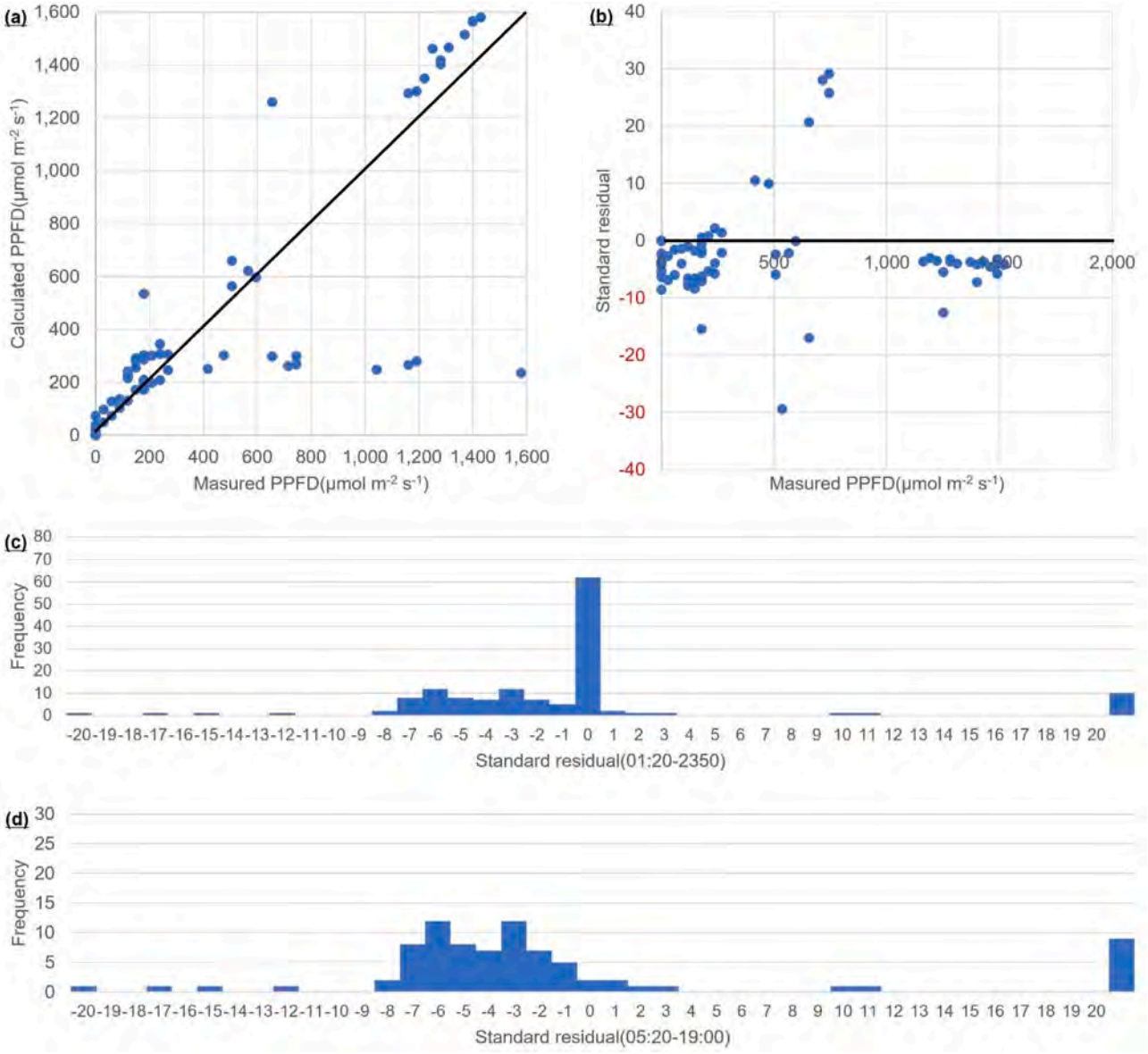

Fig. 20. Standard residual analysis of measured and calculated PPFDs for solar panel angle of 0° in sunny weather on May 29, 2017. (a) Comparison of measured and calculated PPFD; (b) standard residuals of measured and calculated PPFD with measured PPFD on the horizontal axis; (c) frequency of standard residuals between measured and calculated PPFD (01:20–23:50); (d) frequency of standard residuals between measured and calculated PPFD (05:20–19:00).

PPFDd and *PPFDs* were calculated using the model by Tawa et al. The equations for *PPFDd* and *PPFDs* are as follows.

$$\mathrm{PPFDd_{it}} = \frac{cId_t}{N_A h_p c}\left(\left(\sum_{k=15}^{37}\frac{\left(Id_{t_k}+Id_{t_{k+1}}\right)}{2}\left(\lambda_{k+1}-\lambda_k\right)\frac{\left(\lambda_{k+1}+\lambda_k\right)}{2}\right)+\left(\frac{Id_{t_{37}}+Id_{t_{38}}}{2}\left(\lambda_{38}-\lambda_{37}\right)\frac{\lambda_{38}+\lambda_{37}}{2}\right)\right) \quad (23)$$

$$\mathrm{PPFDs}_{it} = \mathrm{PPFD}_{it} - \mathrm{PPFDd}_{it} \quad (24)$$

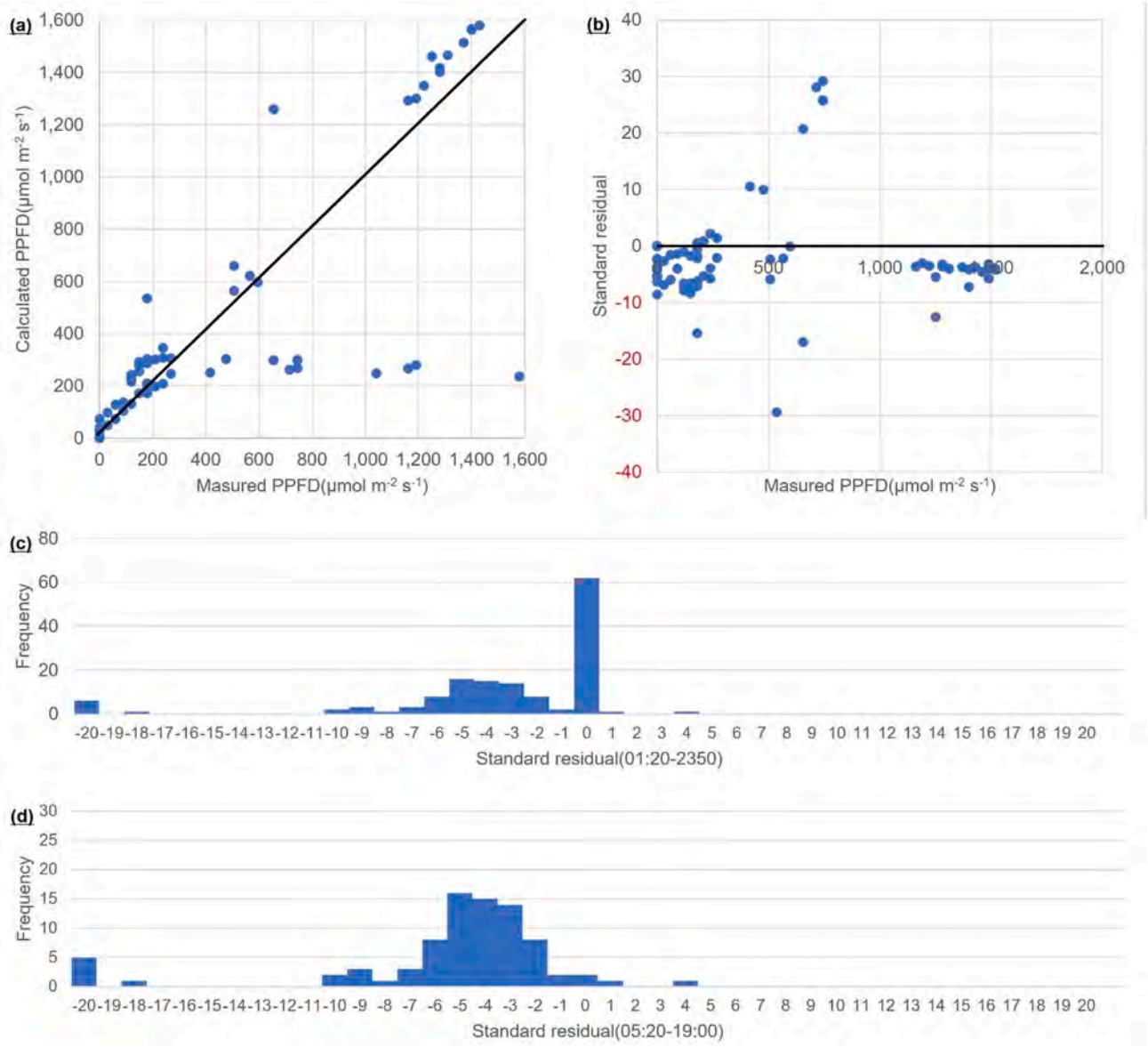

Fig. 21. Standard residual analysis between measured and calculated PPFDs for solar panel angle of 60° in sunny weather on May 29, 2017. (a) Comparison of measured and calculated PPFD; (b) standard residuals of measured and calculated PPFD with measured PPFD on the horizontal axis; (c) frequency of standard residuals between measured and calculated PPFD (01:20–23:50); (d) frequency of standard residuals between measured and calculated PPFD (05:20–19:00).

$$\mathrm{PPFD}_{it} = \frac{cI_t}{N_A h_p c}\left(\left(\sum_{k=15}^{37}\frac{(I_{t_k}+I_{t_{k+1}})}{2}(\lambda_{k+1}-\lambda_k)\frac{(\lambda_{k+1}+\lambda_k)}{2}\right)+\left(\frac{I_{t_{37}}+I_{t_{38}}}{2}(\lambda_{38}-\lambda_{37})\frac{\lambda_{38}+\lambda_{37}}{2}\right)\right) \tag{25}$$

$$cId_t = if\left(sId_t \le 1\frac{W}{m^2},0,\frac{GI_j}{sId_t}\right)(GI_j>0) \tag{26}$$

$$cI_t = if\left(sI_t \le 1\frac{W}{m^2},0,\frac{DI_j}{sI_t}\right)(DI_j>0) \tag{27}$$

$$sId_t = \sum_{k=0}^{Num-2}\frac{(Id_j)_k+(Id_j)_{k+1}}{2}(\lambda_{k+1}-\lambda_k) \tag{28}$$

$$sI_t = \sum_{k=0}^{Num-2}\frac{(I_j)_k+(I_j)_{k+1}}{2}(\lambda_{k+1}-\lambda_k) \tag{29}$$

In the above equations, N_A is Avogadro's number, h_p is Planck's constant, and c is the velocity of light; λ_{15}, λ_{37}, and λ_{38} in the model by Bird and Riordan (1986) (the suffix k originates at 0) correspond to 0.400 μm, 0.690 μm, and 0.710 μm, respectively in Table 2. In original table by Bird and Riordan, the interval between 0.400 μm and 0.550 μm is 0.010 μm; however, after that, the intervals are not equally spaced, such as 0.020 μm and 0.026 μm. Id_t and I_t are elements of the vectors

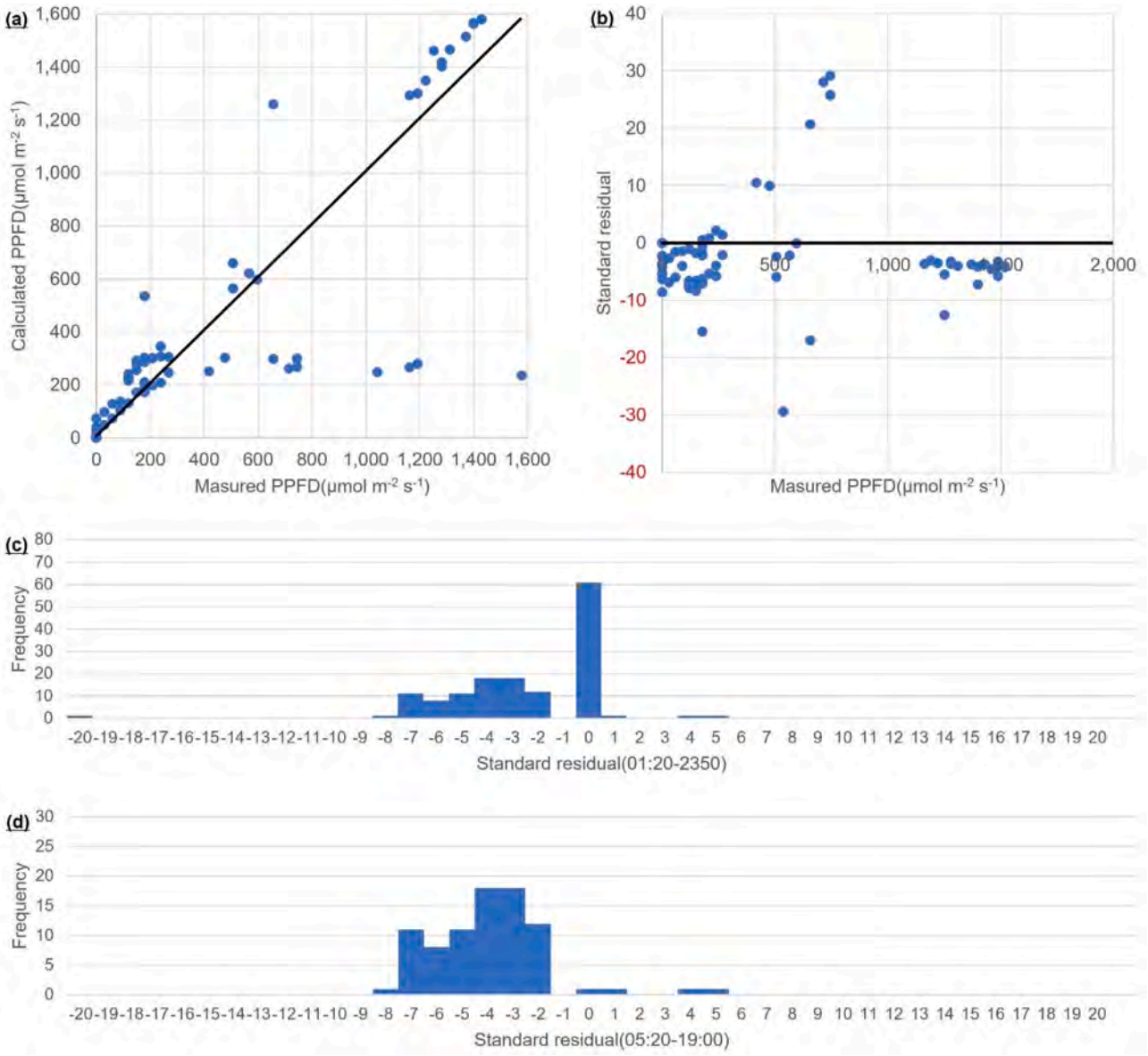

Fig. 22. Standard residual analysis of measured and calculated PPFDs at the observation point not affected by solar panels in sunny weather on May 29, 2017. (a) Comparison of measured and calculated PPFD; (b) standard residuals of measured and calculated PPFD with measured PPFD on the horizontal axis; (c) frequency of standard residuals between measured and calculated PPFD (01:20–23:50); (d) Frequency of standard residuals between measured and calculated PPFD (05:20–19:00).

from the calculated spectrum density in the direct and diffused components of sunlight at a given time/date in the interpolated continuous function, and Id_t and I_t are discrete elements calculated based on the model by Tawa et al. (2020). cId_t and cI_t are the elements of the vectors and scaling factors for the measured spectrum at a given time/date calculated from sId_t and sI_t. *GI* is the measured global horizontal irradiation, and *DI* is the measured direct horizontal irradiation. *Num* is the total number of targeted wavelengths in Table 2 in Bird and Riordan (1986); in this study, *Num* = 122. To avoid division by zero and the expansion of errors through division by small numbers, the spectrum in the time during which the irradiance was less than 1 W/m^2 was filtered. The numerical integration in the weighting by wavelength was performed using the trapezoid formula because other advanced numerical integrations, including Simpson's formula, often become unstable because of sharp transitions caused by the absorption of gases such as ozone.

2.4. Measurements

The University of Miyazaki is continuously monitoring solar resources in various aspects. EKO MS-602 pyranometers were used for monitoring the global total irradiance in the horizontal plane (Fig. 10).

A pyrheliometer (EKO MS-56) with a 2-axis tracker was used to measure the direct normal irradiance (Fig. 11).

The solar spectrum, specifically the global spectrum on the sloped surface, was measured using spectroradiometers (Fig. 12).

The spectrum measurement range was 300–1700 nm by combining two spectroradiometers, and the measurement resolution was 1 nm in the entire wavelength range. The slope angles of the spectroradiometers were 35°. The global spectrum was measured every 10 min from 5:00 a.m. to 8:00 p.m., and the time interval for the simulation was also 10 min. The farmland was horizontal, and the spectrum was converted to horizontal planes using the ACSS model. This study used the measured spectrum to validate the ACCS model. The solar spectrum on the shaded and non-shaded farmland was calculated using the ACSS model based on

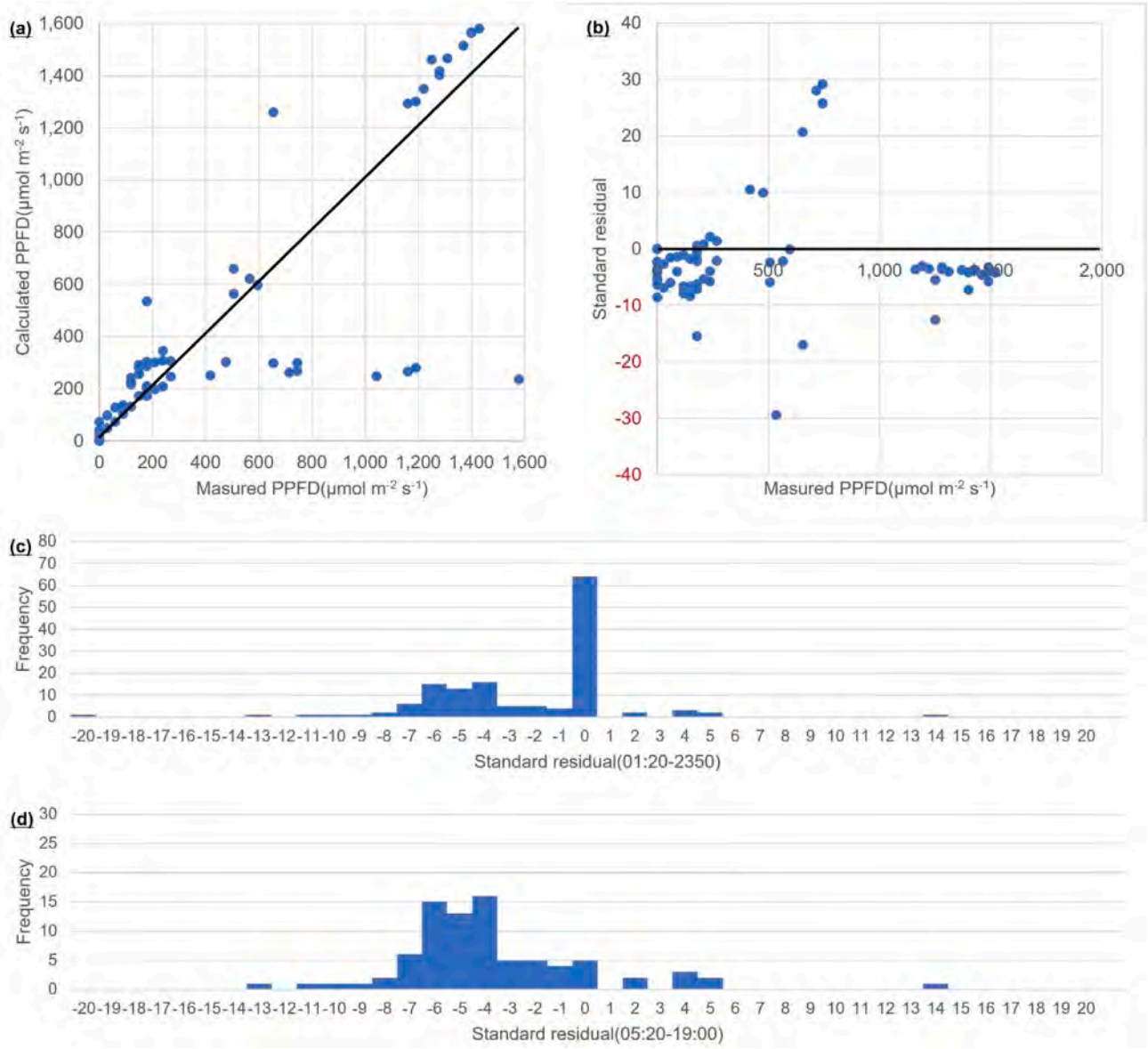

Fig. 23. Standard residual analysis of measured and calculated PPFDs for solar panel angle of 0° in cloudy weather on May 31, 2017. (a) Comparison of measured and calculated PPFD; (b) standard residuals of measured and calculated PPFD with measured PPFD on the horizontal axis; (c) frequency of standard residuals between measured and calculated PPFD (01:20–23:50); (d) frequency of standard residuals between measured and calculated PPFD (05:20–19:00).

the measured values of the horizontal global irradiance and direct normal irradiance, aerosol density (smoothed value of our measurement), water precipitation (smoothed value of our measurement), and calculated solar position (sun height and azimuth angle).

A PPFD sensor (Fig. 13) was used for the measurement of the PPFD (IKS-27 from Koito).

It was similar to a pyrometer with a color filter and domed opaque diffusor and was calibrated using an indoor solar simulator operating in the AM1.5G (ASTM175) spectrum or an incandescent lamp specially manufactured for the calibration of optical instruments. The calibration procedure of the PPFD sensor was related to the inherent error of the PPFD measurement under the variable spectrum. The PPFD measurement was performed from May 16, 2017, to April 06, 2018. The sampling period was 10 min. The solar irradiance measurement acquired every 10 s was averaged every 10 min to adjust the data size in the PPFD calculation. On many days, the data reflected the shadow effect of the crops. In this study, data from two days (sunny weather day and cloudy weather day) considered to be unaffected by the shadowing of the crops were selected and analyzed.

3. Results

The comparison between the measured and calculated PPFDs was performed for a total of six patterns, as shown in Table 3—two observation points under the solar panels tilted at 0° and 60° and one observation point not affected by the solar panels in both sunny and cloudy weather. The sunny weather was on May 29, 2017, and the cloudy weather was on May 31, 2017.

Figures comparing the measured and calculated PPFDs and global total irradiance in the horizontal plane from patterns 1 to 6 are shown in Figs. 14–19.

Pattern 1: Observation point under solar panels with solar panel angle of 0° in sunny weather.

Pattern 2: Observation point under solar panels with solar panel angle of 60° in sunny weather.

Pattern 3: Observation point not affected by solar panels in sunny weather.

Pattern 4: Observation point under solar panels with solar panel angle of 0° in cloudy weather.

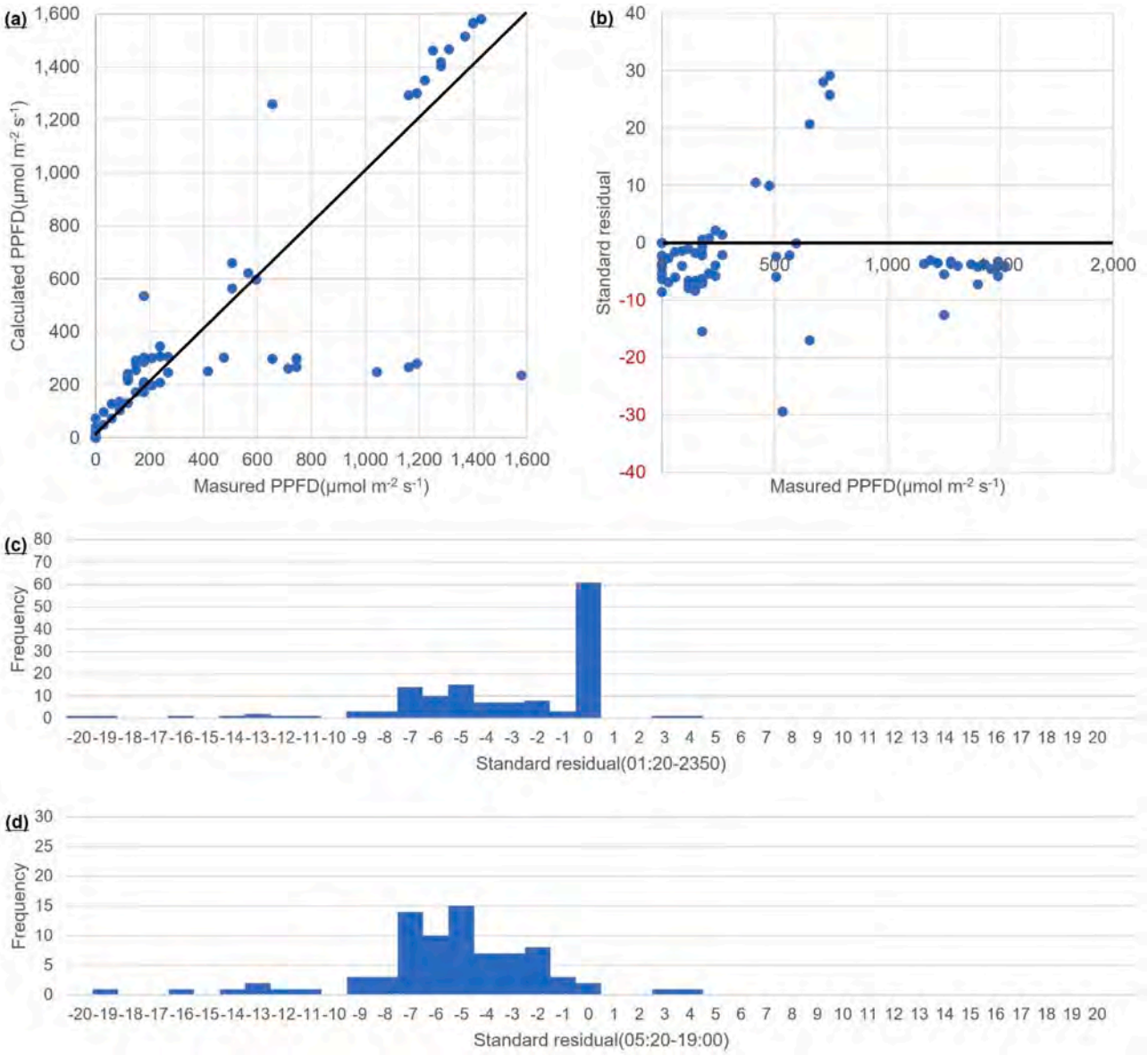

Fig. 24. Standard residual analysis of measured and calculated PPFDs in the case of solar panel angles of 60° in cloudy weather on May 31, 2017. (a) Comparison of measured and calculated PPFD; (b) standard residuals of measured and calculated PPFD with measured PPFD on the horizontal axis; (c) frequency of standard residuals between measured and calculated PPFD (01:20–23:50); (d) frequency of standard residuals between measured and calculated PPFD (05:20–19:00).

Pattern 5: Observation point under solar panels with solar panel angle of 60° in cloudy weather.

Pattern 6: Observation point not affected by solar panels in cloudy weather.

4. Discussion

The measured and calculated PPFD waveforms presented in the previous section show the same tendency in all six patterns. However, even when the amount of solar irradiation was measured for several hours at sunrise, the PPFD under the solar panels remained zero. It is possible that the calculated value did not reflect the effect of the shading material on the eastern side.

To confirm the waveform tendency, standard residual analysis was performed as follows. Because solar irradiation was observed between 05:20 and 19:00, two graphs of the standard residual were created, one between 00:10 and 23:50 and the other between 05:20 and 19:00. This excluded both the measured and calculated values of zero during nighttime in the graph between 05:20 and 19:00.

Pattern 1: Observation point under solar panels with solar panel angle of 0° in sunny weather (Fig. 20).

In the case of pattern 1, the measured PPFDs were observed near 300 and 1500 μmol m^{-2} s^{-1}. The peak of the standard residual was higher than −7 and less than −6, and higher than −4 and less than −3 for the data aggregated between 05:20 and 19:00. The calculated PPFDs tended to be larger than the measured PPFDs.

Pattern 2: Observation point under solar panels with solar panel angle of 60° in sunny weather (Fig. 21).

In the case of pattern 2, the measured PPFDs were observed evenly except at 900 μmol m^{-2} s^{-1}. The peak of the standard residual was higher than −6 and less than −5 when the aggregation was between 05:20 and 19:00. The calculated PPFDs tended to be larger than the measured PPFDs.

Pattern 3: Observation point not affected by solar panels in sunny weather (Fig. 22).

In the case of pattern 3, the measured PPFDs were observed evenly. The peak of the standard residual was higher than −5 and less than −3 when the aggregation was between 05:20 and 19:00. The calculated

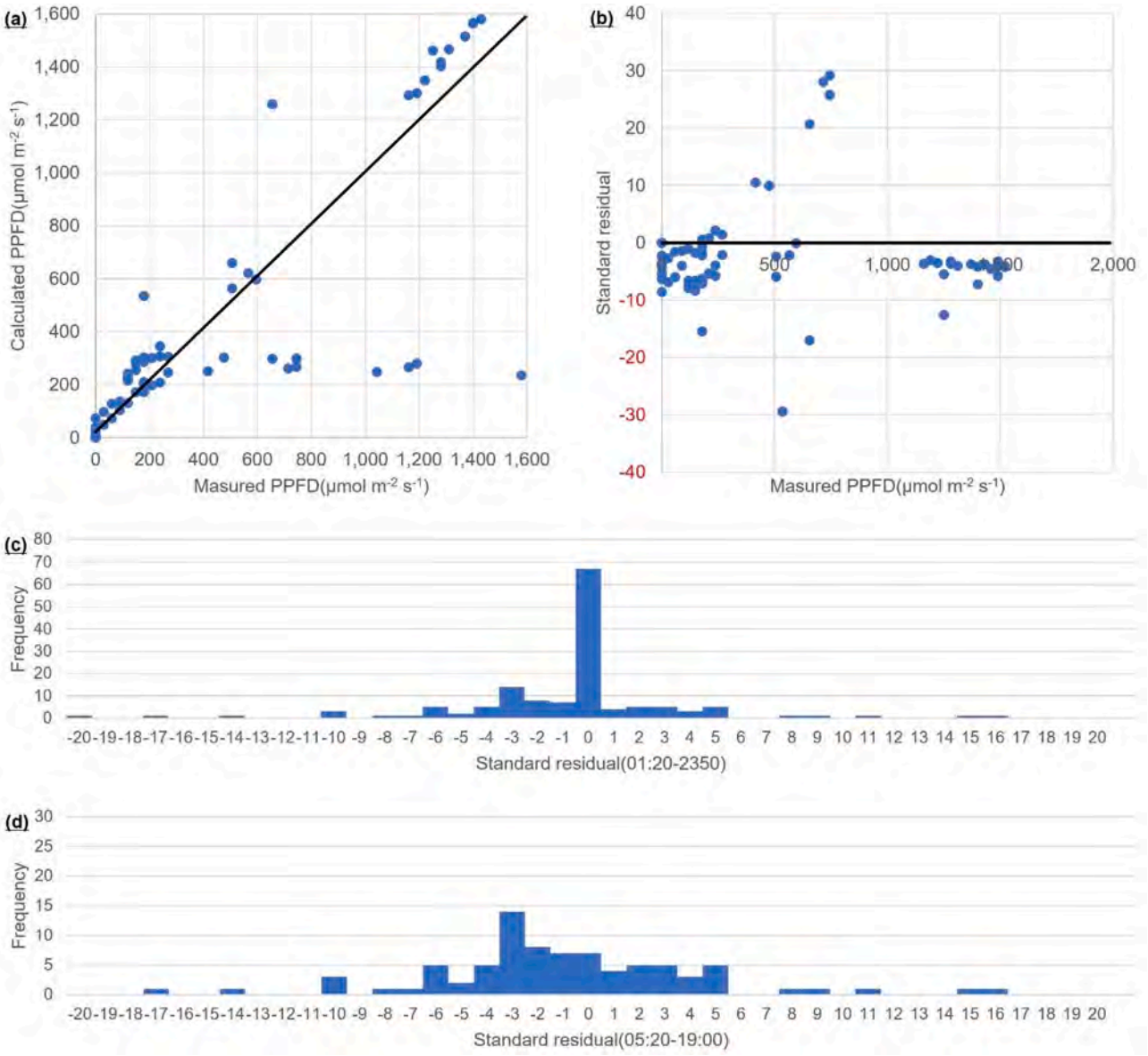

Fig. 25. Standard residual analysis of measured and calculated PPFDs at the observation point not affected by solar panels in cloudy weather on May 31, 2017. (a) Comparison of measured and calculated PPFD; (b) standard residuals of measured and calculated PPFD with measured PPFD on the horizontal axis; (c) frequency of standard residuals between measured and calculated PPFD (01:20–23:50); (d) frequency of standard residuals between measured and calculated PPFD (05:20–19:00).

PPFDs tended to be larger than the measured PPFDs.

Pattern 4: Observation point under solar panels with solar panel angle of 0° in cloudy weather (Fig. 23).

In the case of pattern 4, the measured PPFDs were observed between 0 and 400 μmol m^{-2} s^{-1}. The peak of the standard residual was higher than −5 and less than −4 for the data collected between 05:20 and 19:00. The calculated PPFDs tended to be larger than the measured PPFDs.

Pattern 5: Observation point under solar panels with solar panel angle of 60° in cloudy weather (Fig. 24).

In the case of pattern 5, the measured PPFDs were observed evenly between 0 and 600 μmol m^{-2} s^{-1}. The peak of the standard residual was higher than −6 and less than −5 for the data collected between 05:20 and 19:00. The calculated PPFDs tended to be larger than the measured PPFDs.

Pattern 6: Observation point not affected by solar panels in cloudy weather (Fig. 25).

In the case of pattern 6, the measured PPFDs were observed evenly between 0 and 1100 μmol m^{-2} s^{-1}. The peak of the standard residual was higher than −4 and less than −3 when the aggregation was between 05:20 and 19:00. The calculated PPFDs tended to be larger than the measured PPFDs.

The standard residuals of the six patterns are summarized in Figs. 26 and 27.

In all six patterns, in the case of the frequency graph in which the measured and calculated values include zero during nighttime (00:10–23:50), the peak of the frequency graph will contain zeros. In contrast, in the case of the frequency graph in which the measured and calculated values do not include zero during nighttime (05:20–19:00), the peak moves to the negative side, where it is more prominent than −8 and less prominent than −2 so that the calculated value tends to be estimated higher than the measured value.

Although it is not the subject of this research, the graph below, created with the measured values, summarizes the state of shading owing to the difference in the angle of the solar panels.

A comparison of the angles of the solar panels between 0° and 60° in

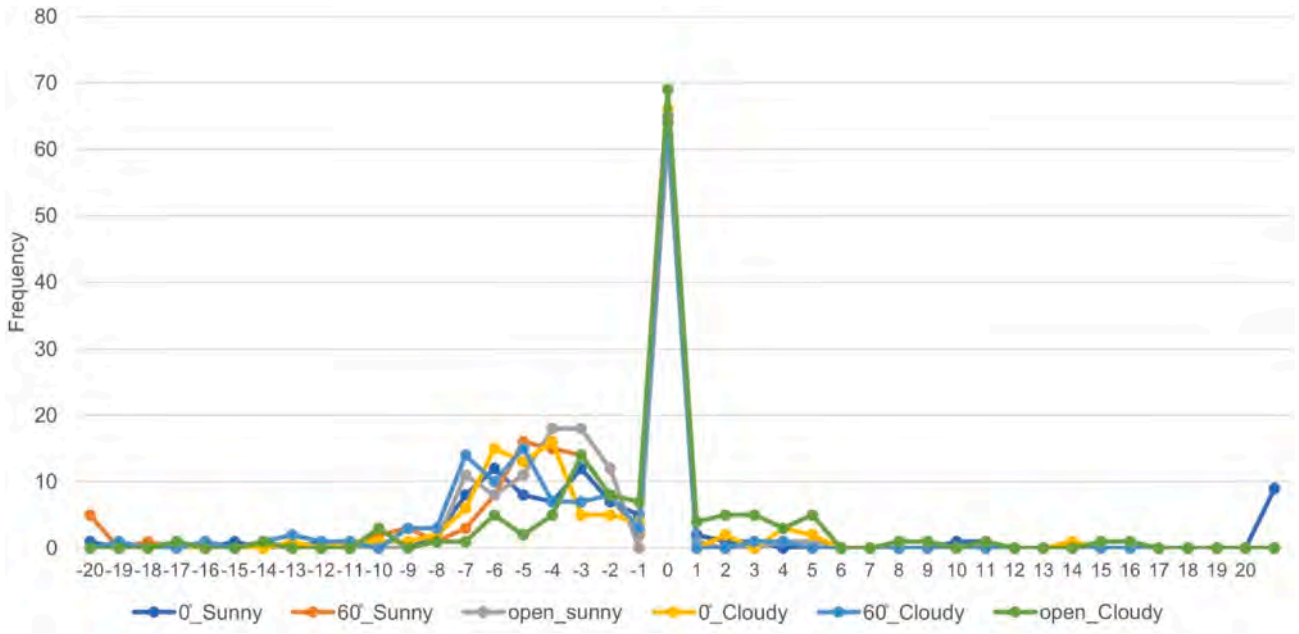

Fig. 26. Summary of the standard residual between 00:10 and 23:50 (sunny weather on May 29, 2017; cloudy weather on May 31, 2017).

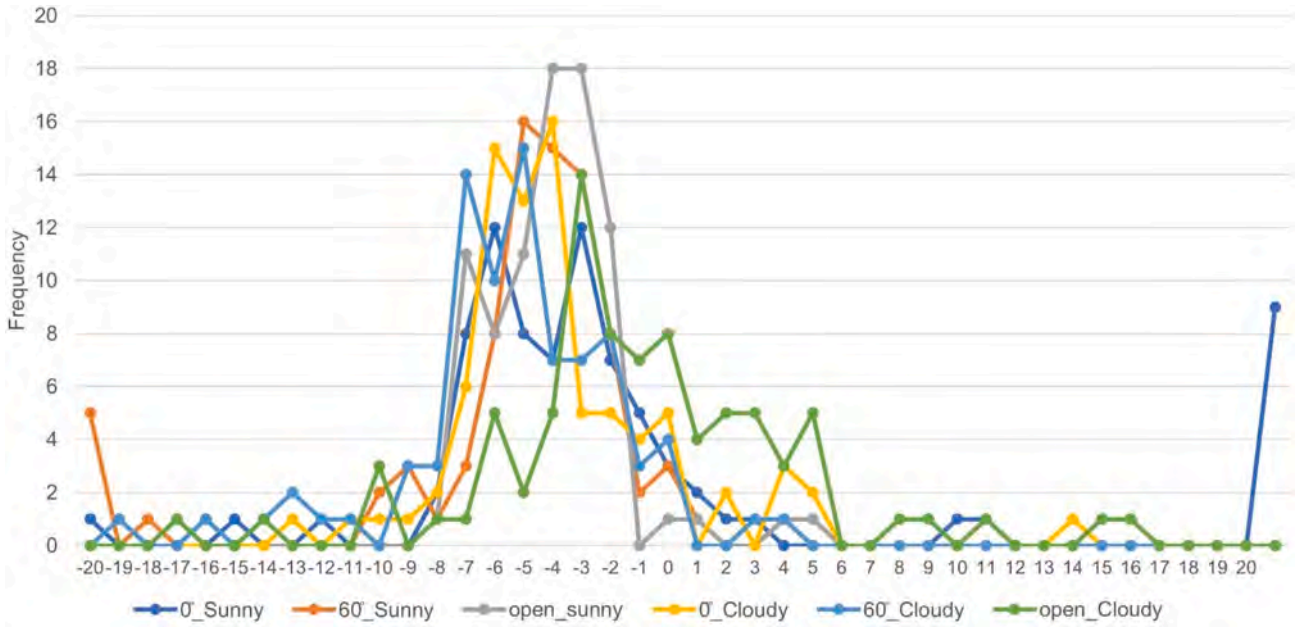

Fig. 27. Summary of the standard residual between 05:20 and 19:00 (sunny weather on May 29, 2017; cloudy weather on May 31, 2017).

the morning (09:00–10:00) and afternoon (14:30–15:30) shows that the angle of 60° supplied 5 to 7 times more PPFD under the solar panels than 0° in Fig. 28. However, in the time period around noon (11:00–12:00, 12:30–13:30), the PPFD obtained at 0° exceeded that obtained at 60°. In the case of cloudy weather in Fig. 29, from 05:20 to 19:00, the amount of solar radiation was almost stable at an average value of approximately 130%.

5. Conclusion

In this study, the calculation formula based on an ACSS model was developed to estimate the PPFD on an agricultural area partially shaded by solar panels and their supporting tubes. The model was validated by comparing the results with actual field measurements. It was found that the waveform based on the calculation formula for the PPFD under the solar panel established in this study reproduced the same tendency as the measured PPFD. The measured and calculated PPFDs were compared using standard residuals to evaluate this trend numerically. The comparisons were for six patterns, considering two weather patterns (sunny and cloudy) each for cases without solar panels and with solar panels tilted at 0° and 60°. In general, a standard residual value between −3 and 3 confirms the similarity between the compared values. All cases in this study resulted in more frequencies with negative standard residual values except for the zero PPFD at night. This indicates that the calculated PPFD tends to be higher than the measured PPFD. The peak frequency of the standard residuals showed six patterns between −6 and −3. This difference probably occurred because the established calculation formula targets the shading provided by the solar panels and

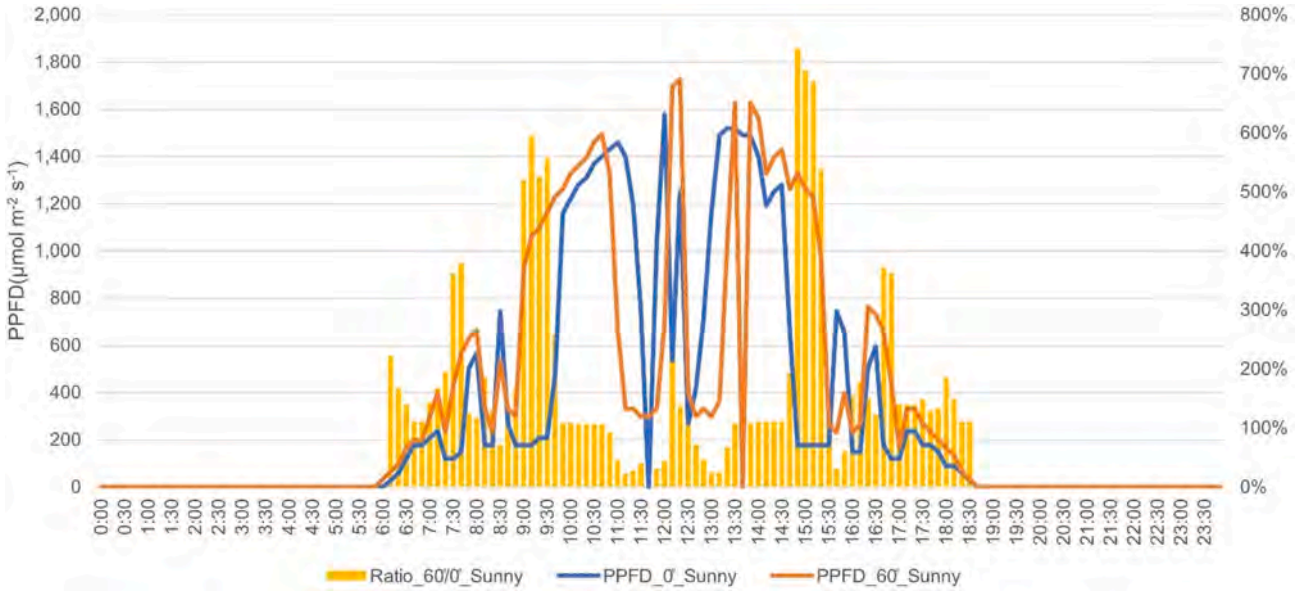

Fig. 28. State of shading in the measured values due to the difference in the angle of the solar panel in sunny weather on May 29, 2017.

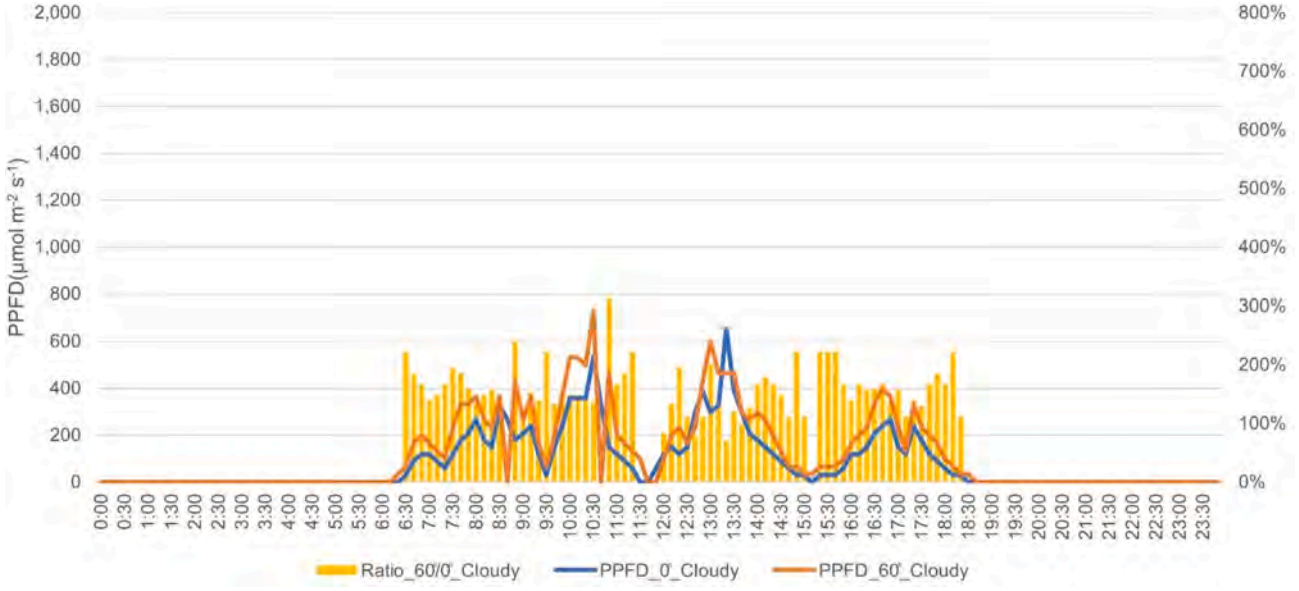

Fig. 29. State of shading in the measured values due to the difference in the angle of the solar panel in cloudy weather on May 31, 2017.

supporting tubes but does not cover the shading provided by the other system structures. Furthermore, the measured PPFD for different elevation angles of the solar panels was compared. The PPFD at an elevation angle of 60° was measured to be approximately 7 times greater than the PPFD at 0° at 15:00 in sunny weather. Even in cloudy weather, the PPFD at an elevation angle of 60° was approximately 2.5 times the PPFD at 0° throughout the day.

The agrivoltaic system allows the simultaneous use of farmland for photovoltaic power generation and agriculture. An appropriate strategy for the optimal sharing of solar resources between solar panels and farmland is valuable. Because the agrivoltaic system is likely to play a significant role in supporting the global challenges of mitigating climate change and increasing food production, the development of an accurate and generalized solar resource calculation method for agricultural products cultivated under the shade of whole system structures such as solar panels and their supporting tubes becomes highly important.

The calculation formula enables farmers to evaluate the economic efficiency of the system before introducing it using measured solar irradiation data at the target farmlands by introducing published neighborhood solar irradiation data and considering, in advance, measures to avoid the effects of shading on agricultural production. The next study will be to improve the accuracy of the calculation formula by increasing the number of days to be analyzed and develop a method that leads to the best practices of agricultural production and solar power generation by introducing the system.

Funding

This work was supported by JSPS KAKENHI Grant Number JP19K06338.

Author statement

Daisuke Yajima: Validation, Writing - Original Draft, Teruya Toyoda:

Data Curation, Masaaki Kirimura: Resources, Kenji Araki: Conceptualization, Methodology, Yasuyuki Ota: Methodology, Kensuke Nishioka: Supervision.

Declaration of competing interest

The authors declare that they have no known competing financial interests or personal relationships that could have appeared to influence the work reported in this paper.

Data availability

Data will be made available on request.

References

Abidin, M.A.Z., Mahyuddin, M.N., Zainuri, M.A.A.M., 2021. Solar photovoltaic architecture and agronomic management in agrivoltaic system: a review. Sustainability 13 (14), 7846. https://doi.org/10.3390/su13147846.

Adeh, E.H., Good, S.P., Calaf, M., Higgins, C.W., 2019. Solar PV power potential is greatest over croplands. Sci. Rep. 9 (1), 11442 https://doi.org/10.1038/s41598-019-47803-3.

Beck, M., Bopp, G., Goetzberger, A., Obergfell, T., Reise, C., Schindele, S., 2012. Combining PV and food crops to agrophotovoltaic–optimization of orientation and harvest. In: 27th European Photovoltaic Solar Energy Conference and Exhibition. EU PVSEC Frankfurt, Germany, pp. 24–28.

Bird, R.E., Riordan, C., 1986. Simple solar spectral model for direct and diffuse irradiance on horizontal and tilted planes at the Earth's surface for cloudless atmospheres. J. Clim. Appl. Meteorol. 25 (1), 87–97. https://doi.org/10.1175/1520-0450(1986)025<0087:SSSMFD>2.0.CO;2.

Braik, A., Makhalfih, A., Sopian, K., Jarimi, H., Ibrahim, A., 2021. Review of agrivoltaics systems potential in Palestine. In: 2021 IEEE Jordan International Joint Conference on Electrical Engineering and Information Technology (JEEIT), pp. 176–180. https://doi.org/10.1109/JEEIT53412.2021.9634128.

Ceran, B., Mielcarek, A., Hassan, Q., Teneta, J., Jaszczur, M., 2021. Aging effects on modelling and operation of a photovoltaic system with hydrogen storage. Appl. Energy 297. https://doi.org/10.1016/j.apenergy.2021.117161, 117161.

Choubchilangroudi, A., Zarei, A., 2022. Investigation the effectiveness of light reflectors in transmitting sunlight into the vertical farm depth to reduce electricity consumption. Clean. Eng. Technol. 7, 100421 https://doi.org/10.1016/j.clet.2022.100421.

Coşgun, A.E., 2021. The potential of agrivoltaic systems in Turkey. Energy Rep. 7, 105–111. https://doi.org/10.1016/j.egyr.2021.06.017.

Cuppari, R.I., Higgins, C.W., Characklis, G.W., 2021. Agrivoltaics and weather risk: a diversification strategy for landowners. Appl. Energy 291, 116809. https://doi.org/10.1016/j.apenergy.2021.116809.

Dupraz, C., Marrou, H., Talbot, G., Dufour, L., Nogier, A., Ferard, Y., 2011. Combining solar photovoltaic panels and food crops for optimising land use: towards new agrivoltaic schemes. Renew. Energy 36 (10), 2725–2732. https://doi.org/10.1016/j.renene.2011.03.005.

Forkuor, G., Amponsah, W., Oteng-Darko, P., Osei, G., 2022. Safeguarding food security through large-scale adoption of agricultural production technologies: the case of greenhouse farming in Ghana. Clean. Eng. Technol. 6, 100384 https://doi.org/10.1016/j.clet.2021.100384.

Gregg, W.W., Carder, K.L., 1990. A simple spectral solar irradiance model for cloudless maritime atmospheres. Limnol. Oceanogr. 35 (8), 1657–1675. https://doi.org/10.4319/lo.1990.35.8.1657.

Hassan, Q., 2020. Optimisation of solar-hydrogen power system for household applications. Int. J. Hydrogen Energy 45 (58), 33111–33127. https://doi.org/10.1016/j.ijhydene.2020.09.103.

Hassan, Q., Jaszczur, M., Abdulateef, A.M., Abdulateef, J., Hasan, A., Mohamad, A., 2022. An analysis of photovoltaic/supercapacitor energy system for improving self-consumption and self-sufficiency. Energy Rep. 8, 680–695. https://doi.org/10.1016/j.egyr.2021.12.021.

Irie, N., Kawahara, N., Esteves, A.M., 2019. Sector-wide social impact scoping of agrivoltaic systems: a case study in Japan. Renew. Energy 139, 1463–1476. https://doi.org/10.1016/j.renene.2019.02.048.

Itagaki, A., Okamura, H., Yamada, M., 2003. Preparation of meteorological data set throughout Japan for suitable design of PV systems. In: 3rd World Conference on Photovoltaic Energy Conversion, 2003. Proceedings of IEEE, 2, pp. 2074–2077.

Kostik, N., Bobyl, A., Rud, V., Salamov, I., 2020. The potential of agrivoltaic systems in the conditions of southern regions of Russian Federation. IOP Conf. Ser. Earth Environ. Sci. 578 (1), 12047 https://doi.org/10.1088/1755-1315/578/1/012047.

Kumpanalaisatit, M., Setthapun, W., Sintuya, H., Jansri, S.N., 2022. Efficiency improvement of oround-mounted solar power generation in agrivoltaic system by cultivation of bok choy (Brassica rapa subsp. chinensis L.) under the panels. Int. J. Renew. Energy Dev. 11 (1), 103–110. https://doi.org/10.14710/ijred.2022.41116.

Moreda, G.P., Muñoz-García, M.A., Alonso-García, M.C., Hernández-Callejo, L., 2021. Techno-economic viability of agro-photovoltaic irrigated arable lands in the EU-Med region: a case-study in southwestern Spain. Agronomy 11 (3), 593. https://doi.org/10.3390/agronomy11030593.

Nordberg, E.J., Caley, M.J., Schwarzkopf, L., 2021. Designing solar farms for synergistic commercial and conservation outcomes. Sol. Energy 228, 586–593. https://doi.org/10.1016/j.solener.2021.09.090.

Pascaris, A.S., Schelly, C., Burnham, L., Pearce, J.M., 2021. Integrating solar energy with agriculture: industry perspectives on the market, community, and socio-political dimensions of agrivoltaics. Energy Res. Social Sci. 75, 102023 https://doi.org/10.1016/j.erss.2021.102023.

Perna, A., Grubbs, E.K., Agrawal, R., Bermel, P., 2019. Design considerations for agrophotovoltaic systems: maintaining PV area with increased crop yield. In: 2019 IEEE 46th Photovoltaic Specialists Conference (PVSC), pp. 668–672. https://doi.org/10.1109/PVSC40753.2019.8981324.

Powell, J.W., Welsh, J.M., Pannell, D., Kingwell, R., 2021. Factors influencing Australian sugarcane irrigators' adoption of solar photovoltaic systems for water pumping. Clean. Eng. Technol. 4, 100248 https://doi.org/10.1016/j.clet.2021.100248.

Randle-Boggis, R.J., Lara, E., Onyango, J., Temu, E.J., Hartley, S.E., 2021. Agrivoltaics in East Africa: opportunities and challenges. AIP Conf. Proc. 2361, 090001 https://doi.org/10.1063/5.0055470.

Schindele, S., Trommsdorff, M., Schlaak, A., Obergfell, T., Bopp, G., Reise, C., Braun, C., Weselek, A., Bauerle, A., Högy, P., Goetzberger, A., Weber, E., 2020. Implementation of agrophotovoltaics: techno-economic analysis of the price-performance ratio and its policy implications. Appl. Energy 265, 114737. https://doi.org/10.1016/j.apenergy.2020.114737.

Tawa, H., Saiki, H., Ota, Y., Araki, K., Takamoto, T., Nishioka, K., 2020. Accurate output forecasting method for various photovoltaic modules considering incident angle and spectral change owing to atmospheric parameters and cloud conditions. Appl. Sci. 10 (2), 703. https://doi.org/10.3390/app10020703.

Tobiska, W.K., Woods, T., Eparvier, F., Viereck, R., Floyd, L., Bouwer, D., Rottman, G., White, O.R., 2000. The SOLAR2000 empirical solar irradiance model and forecast tool. J. Atmos. Sol. Terr. Phys. 62 (14), 1233–1250. https://doi.org/10.1016/S1364-6826(00)00070-5.

Toledo, C., Scognamiglio, A., 2021. Agrivoltaic systems design and assessment: a critical review, and a descriptive model towards a sustainable landscape vision (three-dimensional agrivoltaic patterns). Sustainability 13 (12), 6871. https://doi.org/10.3390/su13126871.

Trommsdorff, M., Kang, J., Reise, C., Schindele, S., Bopp, G., Ehmann, A., Weselek, A., Högy, P., Obergfell, T., 2021a. Combining food and energy production: design of an agrivoltaic system applied in arable and vegetable farming in Germany. Renew. Sustain. Energy Rev. 140, 110694 https://doi.org/10.1016/j.rser.2020.110694.

Trommsdorff, M., Vorast, M., Durga, N., Patwardhan, S.M., 2021b. Potential of agrivoltaics to contribute to socio-economic sustainability: a case study in Maharashtra/India. AIP Conf. Proc. 2361, 040001 https://doi.org/10.1063/5.0054569.

Willockx, B., Herteleer, B., Cappelle, J., 2020. Theoretical potential of agrovoltaic systems in Europe: a preliminary study with winter wheat. In: 2020 47th IEEE Photovoltaic Specialists Conference (PVSC), pp. 996–1001. https://doi.org/10.1109/PVSC45281.2020.9300652.